The structure of the human LACTB filament reveals the mechanisms of assembly and membrane binding

Jeremy A. Bennett[1,¶], Lottie R. Steward[1,¶], Johannes Rudolph[1], Adam P. Voss[1], and Halil Aydin[1,*]

[1]Department of Biochemistry, University of Colorado Boulder, Boulder, Colorado, United States of America

[¶]These authors contributed equally

* halil.aydin@colorado.edu

Abstract

Mitochondria are complex organelles that play a central role in metabolism. Dynamic membrane-associated processes regulate mitochondrial morphology and bioenergetics in response to cellular demand. In tumor cells, metabolic reprogramming requires active mitochondrial metabolism for providing key metabolites and building blocks for tumor growth and rapid proliferation. To counter this, the mitochondrial serine beta-lactamase-like protein (LACTB) alters mitochondrial lipid metabolism and potently inhibits the proliferation of a variety of tumor cells. Mammalian LACTB is localized in the mitochondrial intermembrane space, where it assembles into filaments to regulate the efficiency of essential metabolic processes. However, the structural basis of LACTB polymerization and regulation remains incompletely understood. Here, we describe how human LACTB self-assembles into micron-scale filaments that increase their catalytic activity. The electron cryo-microscopy (cryoEM) structure defines the mechanism of assembly and reveals how highly ordered filament bundles stabilize the active state of the enzyme. We identify and characterize residues that are located at the filament-forming interface, and further show that mutations that disrupt filamentation reduce enzyme activity. Furthermore, our results provide evidence that LACTB filaments can bind lipid membranes. These data reveal the detailed molecular organization and polymerization-based regulation of human LACTB and provide new insights into the mechanism of mitochondrial membrane organization that modulates lipid metabolism.

Introduction

Mitochondria are essential components of eukaryotic cells that communicate cellular needs to ensure optimal cellular function [1]. Although mitochondria play a critical role in energy production, mitochondrial metabolism is multifaceted and supports a variety of cellular functions, including free radical production, ion homeostasis, and biosynthesis of precursors for macromolecules [2]. Unlike most organelles, mitochondria are composed of two membranes: an outer membrane (OM) that interfaces directly with the cytosol, and a morphologically complex inner membrane (IM). The inner membrane separates the intermembrane space (IMS) from the matrix and folds inwards to form cristae [3,4]. This complex double-membrane architecture provides discrete compartments for mitochondria to perform diverse metabolic functions [3]. In addition to their central role in various biochemical pathways, mitochondria are remarkably dynamic organelles that constantly adopt a range of morphologies and are actively transported to specific subcellular locations in response to cellular stressors [5,6].

Mitochondria are a major site for lipid metabolism, where biosynthesis of the phospholipids such as phosphatidylethanolamine (PE), phosphatidylglycerol (PG), and cardiolipin (CL) as well as redox-active lipid coenzyme Q (CoQ, ubiquinone) is facilitated by mitochondrial proteins and protein complexes [7–9]. Mitochondrial lipids are involved in maintaining mitochondrial morphology, cristae development, organelle dynamics, regulation of membrane-associated proteins, mitophagy, and regulated cell death [10,11]. The key phospholipid PE is synthesized *de novo* by phosphatidylserine decarboxylase (PISD), a mitochondrial IM enzyme that converts phosphatidylserine (PS) to PE [11]. The newly synthesized PE is then exported to the endoplasmic reticulum (ER) for further conversion to phosphatidylcholine (PC), the most abundant membrane lipid in eukaryotic cells [11]. Disruption of the orthologous gene *Pisd* in mouse models results in embryonic lethality associated with mitochondrial dysfunction and

57 aberrant mitochondrial morphology [12–14]. Hence, *de novo* synthesis of PE is essential for the
58 efficiency of many subcellular processes and compartmentalization [11].
59
60 In many cancer cells, altered lipid metabolism is among the most prominent metabolic alterations
61 that promote rapid cancer cell growth and tumor formation [15]. Processes that regulate lipid
62 levels are important targets for the differentiation and proliferation of cancer cells [15]. Being at
63 the junction of various metabolic pathways, mitochondrial processes are also associated with
64 tumorigenesis and tumor progression [16]. Although mitochondrial dysfunction and aerobic
65 glycolysis have been widely accepted as hallmarks of cancer, functional mitochondria are also
66 important for tumor growth as active mitochondrial lipid metabolism supports the metabolic needs
67 of highly proliferative cancer cells throughout tumorigenesis [16,17]. Conversely, tumor
68 suppressor proteins can influence the production of lipids by acting through their biosynthesis
69 pathway [18–20]. In mitochondria, the serine beta-lactamase-like protein (LACTB), which is
70 localized in mitochondrial IMS, functions as a tumor suppressor by regulating the PE biosynthetic
71 pathway [20–22]. LACTB is widely expressed in different mammalian tissues, most notably in the
72 skeletal muscle, heart, and liver, and was found to negatively affect the proliferation of a variety
73 of tumor cells *in vivo*, while it exerts little or no effect on the growth of non-tumorigenic cells
74 [20,23]. It has been reported that LACTB expression has been significantly downregulated by
75 promoter methylation, histone deacetylation, and several microRNAs (miRNAs) in various
76 cancers, including breast cancers, uterine cancer, colorectal cancers, gliomas, melanomas,
77 hepatocellular carcinomas, and oxaliplatin-resistant gastric cancer [24–29]. The downregulation
78 of LACTB expression is often correlated with a poor prognosis in these anomalies [28]. While the
79 direct mechanism for tumor suppression by LACTB is unknown, studies have shown that LACTB
80 expression results in reduced PISD protein levels in human breast cancer cells [20].
81 Downregulation of PISD by LACTB is associated with markedly reduced production of PE from

82 PS in carcinoma cells and a decrease in cell proliferation [20]. A possible mechanism for the
83 regulation of PISD by LACTB may involve the formation of micron-scale filaments that control the
84 distance between the inner and outer mitochondrial membranes such that the reaction to form PE
85 by PISD1 is unable to occur due to spatial rearrangement [30]. The downregulation of LACTB
86 mRNA and protein levels by cellular factors would result in reduced protein quantities in
87 mitochondria, hinder filament formation, limit the length of self-assembled filaments, and decrease
88 the catalytic activity of the enzyme *in vivo*; therefore, debilitating its regulatory role in lipid
89 metabolism. Since PE plays an important role in promoting mitochondrial dynamics [14,31,32],
90 the dysregulation of PE homeostasis due to a disruption to the LACTB self-assembly mechanism
91 would be detrimental to mitochondrial function and spatial organization. However, the exact
92 mechanism underlying LACTB on tumor suppression, the association between the
93 downregulation of LACTB gene expression by miRNAs, and the effect on filament formation have
94 yet to be determined. Moreover, mammalian LACTB regulates mitochondrial respiratory complex
95 I activity [33] and participates in cellular metabolic processes [34–36]. Dysregulation of LACTB is
96 associated with obesity and atherosclerosis potentially due to its involvement in metabolic
97 pathways, in particular the phospholipid metabolism in mitochondria [20,34,35]. Given its strong
98 relation to metabolic pathways, *LACTB* is also validated as an obesity gene capable of modifying
99 adiposity [34].
100
101 LACTB is a conserved mammalian active-site serine protease present in all vertebrates [37]. The
102 conserved catalytic serine residue within the ^{164}SXXK^{167} motif plays an important role in the
103 enzymatic activity of LACTB and is reversibly acylated through substrate binding [21,37]. Amino
104 acid sequence analyses show that serine protease LACTB shares sequence similarity to the
105 penicillin-binding protein and β-lactamases (PBP-βLs) family involved in peptidoglycan synthesis
106 [37]. Given that the sequences of β-lactamases are conserved from bacteria to humans, it has

107 been predicted that the molecular mechanisms underlying the cellular function are conserved for
108 β-lactamases across species [37]. However, very little is known about the structural properties
109 and function of LACTB in eukaryotic organisms. In contrast to its prokaryotic homologs, the
110 human LACTB is expressed as a single polypeptide with an N-terminal mitochondrial targeting
111 sequence [22,23]. Furthermore, mammalian LACTB dynamically assembles into filamentous
112 polymers extending more than a hundred nanometers [21]. Filamentation has been observed for
113 a variety of metabolic enzymes and is recognized as a general mechanism for regulating activity
114 [38–45]. For LACTB, the mechanisms by which filament formation modulates enzyme activity
115 remain unclear. Filaments of mammalian LACTB are reported to have a possible structural
116 function in the spatial organization of mitochondrial IMS [21]. Recently, endurance exercise
117 training has been shown to affect the polymerization of LACTB molecules in mice mitochondria
118 suggesting that polymer assembly may have been directly influenced by metabolic activity in cells
119 [36]. The formation of filaments may serve a regulatory function that results in more rapid
120 activation or inhibition of the enzyme in response to changing cellular conditions.
121
122 A structure of a LACTB filament can help elucidate the biochemical characteristics of LACTB and
123 permit a comprehensive mapping of polymerization activity. Here, we describe the atomic-
124 resolution structure of the LACTB filament determined by using cryoEM. The structure reveals the
125 inter-subunit interactions and overall assembly mechanism of LACTB. Furthermore, we provide
126 supporting biochemical analysis of the assembly, where structure-guided mutations at different
127 filament-forming interfaces unveil that polymerization is essential for the catalytic activity of
128 LACTB. Importantly, our work reveals that LACTB exerts its regulatory role by directly interacting
129 with lipid membranes, building a basis for understanding the mechanism of mitochondrial
130 membrane organization. These insights expand our understanding of human LACTB function and

131 lay the foundation for further studies of its dynamic regulation and role in tumor suppression and

132 metabolism.

133

134 # Results

135 **Functional characterization of human LACTB filaments.** To examine the molecular
136 architecture of human LACTB, we purified near full-length LACTB (residues 97-547) lacking the
137 N-terminal targeting sequence (Fig 1A-C). The protein was fractionated further with Superose 6
138 Increase size-exclusion chromatography (SEC), wherein a single peak corresponding to a large
139 molecule was observed on the elution profile indicating the formation of high-molecular-weight
140 species (Fig 1D). These oligomers seemed to be dynamic, as illustrated by the asymmetric and
141 tailing peak on the gel filtration column (Fig 1D). Analysis of the chromatogram peak using
142 negative-stain transmission electron microscopy (TEM) revealed that LACTB assembled into
143 filaments of several hundred nanometers in size (Fig 1E). Our initial observations suggested that
144 the polymers consisted of repeating LACTB subunits, resulting in flexible filaments with an outer
145 radius of 150 Å and a wide range of length distribution (Fig 1E). To test the proteolytic activity of
146 LACTB filaments, we performed an *in vitro* substrate assay with the fluorogenic Ac-YVAD-AMC
147 peptide and readily detected the enzymatic activity of purified wild-type (WT) LACTB in the
148 polymerized state (Fig 1F). These results confirm that, like the other metabolic enzymes that self-
149 assemble into filaments to organize and regulate metabolism [38,42,43], LACTB subunits can
150 also form catalytically active filaments in solution.

151

152 **Fig 1. Human LACTB assembles into a filament.** (**A**) Domain organization of full-length human
153 LACTB and the construct used in the study. The color scheme is used throughout the manuscript.
154 (**B**) Schematic diagram for recombinant expression and self-assembly of LACTB. (**C**) Coomassie-
155 stained SDS-PAGE of purified LACTB filament. (**D**) Size-exclusion profile of WT LACTB using a
156 Superose 6 column. SEC elution profile begins with the void volume (V_0) of the column. (**E**)
157 Representative negative-stain TEM image of purified samples containing high molecular weight
158 species. Negative-stain TEM analysis is shown for the samples taken from the primary peak

159 observed in the size-exclusion chromatogram and is highlighted with a red box in **C**. Scale bar,
160 100 nm. (**F**) Activity of the purified LACTB filaments was determined by using a fluorescence-
161 based assay with the error bars representing the standard error of the mean (s.e.m.). Source data
162 for (**F**) is provided in sheet Fig 1F in S1 Data.
163
164 **LACTB assembles into a helical filament.** To establish the structural basis for the LACTB
165 filament assembly, we used cryoEM analysis. Initial cryoEM micrographs presented substantial
166 challenges with respect to filament flexibility and clustering under cryogenic conditions. Sample
167 preparation was subsequently optimized by adding detergent for cryoEM grid preparation. The
168 two-dimensional (2D) classifications of overlapping filament segments and initial three-
169 dimensional (3D) reconstructions encompassing multiple protomers revealed the helical
170 architecture of the filament (S1 Fig). After excluding low-quality segments, focus classification
171 and refinement of the central region was carried out with 58% of segments, which reduced
172 heterogeneity and improved map quality (S2 Fig). A final cryoEM reconstruction of the LACTB
173 filament was obtained at an overall resolution of 3.1 Å with an imposed helical symmetry (S2 Fig
174 and Table 1). A map with no noticeable differences (3.1 Å) was obtained when the final subset of
175 segments was refined without imposing helical symmetry indicating that the helical assembly is
176 highly symmetric (S3 Fig). The resulting map quality was sufficient for unambiguous assignment
177 of individual subunits, and to build an atomic model of the complete structure of the LACTB
178 filament (Fig 2 and Table 1). Except for the flexible loop region of the LACTB (residues 243 to
179 290), which extends to the solvent, all secondary structural elements and most side chain
180 densities were clearly resolved in the cryoEM map (Fig 2). The flexible loop (L6) may be weakly
181 resolved due to conformational changes between protomers or because it is mostly disordered
182 and thus cannot be modeled. Further analysis of the structural data revealed that the basic

183 building blocks of LACTB are dimers, which are stacked on each other and assembled into
184 filaments with a helical twist of 48.25° and a rise of 21.63 Å (Fig 2A).

185

186 **Fig 2. CryoEM structure of human LACTB filament.** (**A**) CryoEM images of helical LACTB
187 filaments were processed to obtain the 3D reconstruction of the polymer. LACTB protomers are
188 colored differently, and filament rise and twist are indicated. (**B**) Top view of the LACTB assembly
189 with the indicated filament width and inner lumen diameter. (**C**) Ribbon diagram of LACTB
190 monomer. The chain is colored in a rainbow gradient from N-terminus (blue) to C-terminus (red).
191 Secondary structure elements of one protomer are labeled. (**D**) LACTB (residues 97-547) α-
192 helices (cylinders), β-sheets (arrows), and loops (lines) are depicted in a topology diagram.

193

194 **Table 1 | CryoEM data collection, refinement, and validation statistics**
195

	Human LACTB (EMD-26595) (PDB 7ULW)
Data collection and processing	
Microscope	FEI Titan Krios
Camera	Gatan K3 Summit
Magnification	29,000x
Voltage (kV)	300
Electron exposure (e^-/Å^2)	65
Defocus (μm)	-0.5 to -1.5
Pixel size (Å)	0.8211
Symmetry imposed	Helical
Micrographs (no.)	7643
Initial segment images (no.)	430,592
Final segment images (no.)	248,548
Map resolution (Å)	3.09
FSC threshold	0.143
Map resolution range (Å)	3.1 to 5.8
Refinement	
Initial model used	*de novo*
Model resolution (Å)	2.84
FSC threshold	0.143
Map sharpening *B* factor (Å^2)	-87.6

Model composition	
Nonhydrogen atoms	18766
Protein residues	2400
B factors (Å^2) - min	
Protein	78.60
R.m.s. deviations	
Bond lengths (Å)	0.002
Bond angles (Å)	0.406
Validation	
MolProbity score	1.07
Clashscore	2.84
Poor rotamers (%)	0.00
Ramachandran plot	
Favored (%)	98.74
Allowed (%)	1.26
Disallowed (%)	0.00

Molecular architecture of human LACTB. LACTB has a globular structure with approximate dimensions of 60 Å X 55 Å X 45 Å and consists of a five-stranded β-sheet core (β1, β2, β7, β8, and β9) surrounded by two short two-stranded antiparallel β-sheets (β3 - β4 and β5 - β6) and ten α-helices (α1 - α10) (Fig 2C and 2D). The β-sheet core is flanked by two helices (α1 - α10 and α2 - α8) on either side, creating a compact structure that forms the catalytic core (Fig 2D). These α-helices and the β-sheet core are primarily stabilized by a network of hydrophobic interactions. While the α1 and α10 helices are connected to the β-sheet core with short loops, a 21-residue loop (L3) spans across the β-sheet core to link β2 to α2, and another long loop (L11) resides between the β4 strand and the α8 helix (Fig 2C and 2D). The α-helices, α3-α7 and α9, do not directly interact with the β-sheet core and form the outer surface of the filamentous assembly (Fig 2C). Many charge-charge interactions stabilize the α-helices and the long loops of LACTB. Consistent with these observations, a Dali server search identified several prokaryotic and archaeal PBP-βL family of enzymes, such as ClbP (yellow, PDB ID: 4GDN), Pab87 peptidase (orange, PDB ID: 2QMI), Penicillin-binding protein (pink, PDB ID: 3TG9), and D-amino-acid amidase (purple, PDB ID: 2EFU), as close structural homologs of LACTB (S4 Fig). While the

212 resemblance in the overall fold of LACTB to prokaryotic homologs suggests the conservation of
213 the enzymatic core, significant differences are observed in the loops and α-helices that surround
214 the core structure (S4 Fig). Most importantly, the LACTB monomer includes a long L15 loop
215 (residues 467 to 482) formed between β6 and β7 strands, a helix α4 (residues 227 to 242) that
216 extends in parallel with the β-sheet core, and the predicted flexible loop (residues 243 to 290), all
217 of which are not observed in other PBP-βLs proteins (S4 Fig). Our 3.1 Å map also enabled the
218 identification of the amino acid motifs (^{164}SISK^{167}, ^{323}YST^{325}, and ^{485}HTG^{487}) that contribute to the
219 formation of the catalytic site, including the catalytic S164 residue, all of which are conserved
220 across metazoan species (S5 Fig). The structure highlights a clearly defined cavity, which has a
221 predominantly positively charged character (S5B Fig). The LACTB binding pocket is a ~20 Å deep
222 cavity with a wider outer diameter (~20 Å) and a narrower inner diameter (~10 Å) near the catalytic
223 site (S5A and S5B Fig). In addition to the conserved active site residues, several positively
224 charged (H216, H222, and K394) and aromatic residues (Y223, W454, and Y460) are in close
225 proximity to the catalytic site (S5 Fig). This suggests that LACTB substrates largely dock through
226 charge-charge interactions, with a few polar residues responsible for the catalytic activity.

227

228 **LACTB dimer interface governs filament assembly.** We next sought to establish the
229 mechanism of filament assembly. The LACTB filaments assemble as stacked antiparallel dimers,
230 where the buried surface area between the two protomers (A and B) is ~945 Å^2 (Fig 3A). The
231 structure shows that the antiparallel arrangement between two LACTB monomers results in
232 symmetric interactions between two main dimer interfaces located on the L3 and L9 loops (Fig
233 3A). Assembly of the LACTB dimer is mediated by the combined effects of sixteen hydrogen bond
234 interactions between E149, N150, N364, E365, P366, I368, N370, R371, N385, and T386
235 residues, and two inter-molecular salt bridges between E149 and R371 (Fig 3B). Conservation of

236 these residues across mammalian species suggests that they may play an important role in
237 subunit interactions (S5C Fig). Consistently, mutations targeting the dimer interface, including
238 E149R-N150A double mutant and I368A-N370A-R371E triple mutant completely abolished the
239 dimerization propensity as well as the filament formation of LACTB and produced a peak
240 appearing at a lower molecular weight corresponding to a monomer in SEC analysis (Fig 3C).
241 Additionally, SDS-PAGE analysis and negative-stain electron micrographs of the peak fractions
242 further confirmed our observations on the sizing column and showed that these substitutions
243 remarkably destabilize the local complementary interactions and thus hamper the filament
244 formation (Fig 3C). On the other hand, mutation of N364A-E365A only modestly affected the
245 overall filament stability and showed a gel filtration profile similar to the WT (Fig 3C). Because the
246 N364A-E365A double mutant did not completely hinder filament formation, we predicted that the
247 dimer interface is likely stabilized by multiple polar and electrostatic interactions. To understand
248 how filament assembly and disassembly influence the catalytic activity of LACTB, we
249 characterized the activity of dimerization mutants in substrate assays. Compared to the WT
250 LACTB, the dimer interface mutants, E149R-N150A and I368A-N370A-R371E, were completely
251 inactive, while the N364A-E365A mutation only led to a 20% reduction in LACTB activity (Fig 3D).
252 The negative effect of every dimer interface mutation disrupting the filament assembly suggests
253 that dimerization and subsequent polymerization are necessary to achieve maximal catalytic
254 efficiency. These data provide a mechanism by which the strong interactions between the
255 opposing dimer interface loops promote filament growth and result in increased enzyme activity
256 by stabilizing the active architecture of the catalytic site. Taken together, we can confirm that the
257 LACTB homodimers are the basic building blocks of the filaments, and polymerization is strongly
258 correlated with optimal enzyme activity.

259

260 **Fig 3. Structural characterization of LACTB dimerization interface.** (**A**) LACTB protomers
261 (colored in green and lilac) form an antiparallel dimer as shown in ribbon representation. Residues
262 that are critical for oligomerization are represented in sticks. Black boxes indicate the position of
263 dimer interface residues. (**B**) Zoomed in view of the black box in **A**, showing the interactions that
264 stabilize the dimer formation. The polar and charge-charge interactions are indicated by black
265 and red dotted lines, respectively. (**C**) Size-exclusion chromatography (SEC) elution profiles of
266 WT and mutant LACTB. SEC elution profiles begin with the void volume (V_0) of the column.
267 Fractions were analyzed by SDS-PAGE and peak fractions used in negative-stain TEM analyses
268 are highlighted with red boxes. Negative-stain TEM images demonstrate the polymerization
269 activity of WT and mutant proteins. Scale bars, 100 nm. (**D**) Mutation of key residues involved in
270 dimerization disrupts catalytic activity. Enzyme activity was determined *in vitro* by using a
271 fluorescently labeled substrate and three independent experiments were performed for each
272 sample. Bars represent the mean of at least three independent experiments and error bars
273 represent the standard deviation. The underlying data in (**D**) is provided in sheet Fig 3D in S1
274 Data.

275

276 **LACTB filament elongation is mediated by multiple polymerization interfaces between**
277 **subunits.** When we evaluated multiple LACTB homologs, we decided to focus our structural
278 analysis on the unique polymerization mechanism that brings the LACTB homodimers together
279 to form the full filament. Polymerization is mediated by the association between two LACTB
280 homodimers (protomers A-B and C-D), where 48.25° helical rotation between stacked
281 homodimers is necessary for growing a filament at either end (Fig 4A). The inspection of the inter-
282 dimer interface shows that three assembly contacts between neighboring subunits (A and C, A
283 and D, and B and D) bridge antiparallel LACTB homodimers and drive filament assembly (Fig

284 4A). The first polymer interface, which spans a buried solvent-accessible surface area of ~780
285 Å^2, is formed between the α1 helix and L3 along with the protruding L10 loop between β3 and β4
286 strands of protomers A and D (Fig 4A and 4B). The two-fold symmetric interactions between
287 protomers A and D from neighboring homodimers result in identical electrostatic surface
288 potentials on both sides of the inter-dimer interface (Fig 4A and 4B). Major contacts of this
289 interface include several non-covalent interactions between residues D113, R117, E121, V122,
290 R151, Y377, R382, L383, and S527, and a pair of symmetrical salt bridges between D113, D120,
291 and R151 (Fig 4A and 4B). To verify the functional relevance of these interactions for
292 polymerization and catalytic activity, we performed mutagenesis studies on residues R117, R151,
293 and Y377. Both R117E and R151E charge-reversal mutations hindered the ability of LACTB to
294 assemble into stable elongated filaments and yielded shorter assemblies containing a few LACTB
295 protomers (Fig 4D). Notably, the R151 salt bridge mutation reduced the proteolytic activity of
296 LACTB by ~60% in substrate assays, whereas the R117E mutation only mildly affected the
297 enzyme activity (Fig 4E). Moreover, mutation of the conserved contact site residue Y377 to a
298 lysine did not show major changes in filament length and formation compared to the WT but
299 resulted in a greater effect (~70% reduction) regulating protease activity (Fig 4D and 4E). These
300 characteristics, together with the disruptive effect of charge-reversal mutations, indicate that
301 complementary electrostatic forces stabilize the interactions between stacked LACTB dimers
302 during filament formation.

303

304 **Fig 4. Structural basis of LACTB filament assembly.** (**A**) Ribbon diagram of LACTB tetramer.
305 LACTB protomers are colored in green (A), lilac (B), orange (C), and pink (D). Residues that are
306 critical for oligomerization are represented in sticks. Black boxes indicate the position of the
307 residues located at both polymerization interfaces 1 and 2, respectively. (**B** and **C**) Zoomed in
308 view of polymer interfaces 1 and 2, respectively, showing the interactions that facilitate the

309 polymerization of human LACTB. The polar and charge-charge interactions are indicated by black
310 and red dotted lines, respectively. (**D**) Size-exclusion chromatography (SEC) elution profiles of
311 WT and mutant LACTB. SEC elution profiles begin with the void volume (V_0) of the column.
312 Mutations to residues that are located at the polymerization interfaces 1 and 2 impair
313 filamentation. Fractions were analyzed by SDS-PAGE and peak fractions used in negative-stain
314 TEM analyses are highlighted with red boxes. Negative-stain TEM images demonstrate the
315 polymerization activity of WT and mutant proteins. Scale bars, 100 nm. (**E**) Mutation of key
316 residues involved in filament formation disrupts catalytic activity. Enzyme activity was determined
317 *in vitro* by using a fluorescently labeled substrate and three independent experiments were
318 performed for each sample. Bars represent the mean of at least three independent experiments
319 and error bars represent the standard deviation. The source data from (**E**) is provided in sheet
320 Fig 4E in S1 Data.

321

322 The filament structure also shows a second polymer interface that has symmetric contact sites
323 between protomers A and C and B and D, which bury ~540 $Å^2$ of solvent-accessible surface area
324 (Fig 4A). These two interfaces are formed by the same residues and the interactions are mainly
325 mediated by the charge complementarity and salt bridges (Fig 4A-C). In our filament structure,
326 the unique L15 loop that extends between β6 and β7 strands is embedded within the large pocket
327 formed by α7 and α8 helices and the L12 loop of the adjacent LACTB protomer (Fig 4A-C). The
328 most intimate contacts occur between L15 loop residues Y473, G474, S475, C476, and R477,
329 and the conserved residues H352, D353, D355, Y369, A413, Y416, P432, and Y434 that line the
330 surface of the pocket (Fig 4C). Additional inter-molecular salt bridges are formed between H352
331 and E457, and D355 and R477, which stabilize the filament formation (Fig 4C). To assess the
332 importance of these interfaces, we produced a LACTB construct in which the L15 loop (V467 to

333 Y482) is replaced by a glycine-glycine-serine (GGS) linker to disrupt the helical assembly
334 interface. This mutant impaired the ability of LACTB to form long filaments, as judged using size-
335 exclusion chromatography and negative-stain TEM (Fig 4D). We then tested this construct in
336 substrate assays to measure catalytic activity. Not surprisingly, the removal of the L15 loop
337 completely abolished the enzymatic activity of the purified LACTB oligomers (Fig 4E). Mutations
338 of individual L15 loop residues also hindered the enzymatic activity of LACTB. Substitution of
339 residue G474 with tyrosine markedly reduced the catalytic activity of LACTB by ~85%, whereas
340 charge-reversal mutation of R477 residue resulted in abrogation of catalytic function *in vitro* (Fig
341 4E). We also characterized the role of the inter-molecular charge-charge interactions at the
342 interface. Mutations targeting interface salt bridges, including H352A and D355K, did not affect
343 the filament formation but decreased the enzymatic activity of LACTB by ~60% to 80%,
344 respectively (Fig 4D and 4E). Although these interface residues do not appear to participate in
345 catalytic site formation as they are distant from the active site, they facilitate inter-subunit
346 interactions that increase the stability and catalytic activity of the filament. Interestingly, a
347 structural comparison of the human and prokaryotic PBP-βL family of enzymes unveiled that the
348 LACTB structure is distinguished from its prokaryotic homologs by the addition of the 14-residue
349 L15 loop, which is involved in filament assembly (S4 Fig). Moreover, multiple sequence alignment
350 of the human LACTB and PBP-βL family of enzymes demonstrated very little sequence similarity
351 for amino acids forming the L15 loop (S4E Fig). Consistent with our functional analysis, the L15
352 loop emerges as a regulatory element that controls not only the polymerization but also the
353 catalytic activity of LACTB. Altogether, these results demonstrate that assembly of the filament
354 and the L15 loop are required for catalytic activation of LACTB.

355 We next tested the possibility that changes in reactive oxygen species (ROS) in the mitochondrial
356 IMS may influence the assembly of LACTB filaments. Mitochondrial ROS regulate a wide variety
357 of cellular processes and are linked to multiple pathologies [46,47]. It was previously shown that

358 hydrogen peroxide (H_2O_2) can disarrange actin polymers to provoke cell death during
359 inflammation [48]. H_2O_2 has also been linked to the regulation of mitochondrial membrane
360 morphology and processes of fusion/fission by changing the oligomeric state or monomeric
361 structure of redox-sensitive proteins [49–51]. In our cryoEM structure, we identified a methionine-
362 rich region, where more than half of the methionine residues in LACTB are clustered in this region
363 (S6A Fig). We thus postulated that these methionine residues may be sensitive to H_2O_2-mediated
364 oxidation, which could disrupt filament assembly. To investigate the impact of mitochondrial ROS
365 on LACTB, we exposed protein samples to varying concentrations of H_2O_2 (0.01% to 1%) and
366 showed that LACTB samples oxidized with H_2O_2 migrate more slowly than the native protein as
367 deduced by SDS-PAGE analysis (S6B Fig). Subsequently, we confirmed the oxidation of these
368 methionine residues upon exposure to H_2O_2 by liquid chromatography with tandem mass
369 spectrometry (LC-MS/MS) (S6C Fig). Finally, negative-stain TEM imaging of protein samples
370 revealed that oxidation at higher H_2O_2 concentrations hinders the filament formation of LACTB
371 (S6D Fig). These data suggest that the H_2O_2-mediated oxidation of the protein could alter LACTB
372 self-assembly dynamics and inhibit polymerization *in vitro*.

373

374 **Mechanism of LACTB membrane organization.** LACTB has been shown to localize to the
375 mitochondrial IMS, where it assembles into polymers to regulate lipid metabolism [20–22]. The
376 structure of the LACTB filament can inform its mechanism of action and interactions with lipid
377 membranes. To investigate whether there is a link between mitochondrial membrane organization
378 and LACTB filament formation, we reconstituted freshly purified LACTB with liposomes that
379 closely mimic the lipid composition of mitochondrial inner membranes in a buffer of physiological
380 ionic strength and visualized binding *in vitro*. When analyzed by negative-stain TEM, we directly
381 observed the interplay between LACTB and lipid membranes (Fig 5). LACTB filaments exhibited
382 well-ordered, tightly packed conformation, and appeared to interact with liposomes via the tip of

383 the polymer (Fig 5A). These filaments were often attached to two different liposomes on opposite
384 ends forming a bridge between the two lipid membranes (Figs 5B-E and S7D). Intriguingly, we
385 also identified filaments that interact with liposomes from the side, where multiple protomers form
386 intimate interactions with lipid membranes on either side (Figs 5C-D and S7D). This second
387 binding mode allows LACTB filaments to accommodate different membrane topologies and tightly
388 associate with surrounding membranes, which enables membrane organization. These
389 observations complement data that were previously obtained *in situ* [21], indicating that
390 recombinant LACTB generates biologically relevant assemblies and binds membranes *in vitro*
391 (Fig 5). To further characterize the molecular details of protein-lipid interactions, we first measured
392 the enzymatic activity of LACTB in the presence of CL-containing liposomes and uncovered that
393 membrane binding does not affect the catalytic activity of LACTB filaments (Fig 5G).
394 Subsequently, we prepared liposomes with four different lipid compositions to test the effect of
395 mitochondrial IM lipids on LACTB activity (S7A Fig). We observed an average two-fold decrease
396 in liposome binding when we omitted CL from lipid vesicles (S7B-C Fig). Moreover, human LACTB
397 filaments facilitate mitochondrial membrane organization, which requires these filaments to form
398 stable interactions with two distinct membrane regions and coordinate their spatial organization
399 [21]. To assess this activity *in vitro*, we also calculated the percentage of filaments that appeared
400 to be tethered to two or more liposomes and observed a four-fold decrease in the tethering activity
401 of LACTB filaments in the absence of CL (Fig 5H). We also determined whether LACTB filaments
402 can sense regions of high membrane curvature that may be important for membrane remodeling
403 processes. Specifically, we prepared CL-containing cylindrical liposomes that form membrane
404 tubules and provide curved membrane surfaces. The reconstitution assays with cylindrical
405 nanotubes revealed that LACTB filaments have a stronger affinity to cylindrical nanotubes than
406 spherical vesicles (S7E). Together, these results indicate that CL and positively curved
407 membranes enhance the membrane binding activity of human LACTB.

408

409 Furthermore, we postulated that the flexible loop region between residues 243-290 could facilitate
410 membrane binding. Specifically, the human LACTB sequence contains a charged and
411 hydrophobic motif (^{259}KNxFxKFK^{266}) as well as a cluster of six basic side chains
412 (^{274}KxRxxKxxKKK^{284}) with a remarkably electropositive character within this region that may form
413 interactions with CL-containing liposomes *in vitro* (S5C Fig). To define the molecular determinants
414 of membrane binding, we replaced the flexible loop region (residues K255 to K284) with a glycine-
415 glycine-serine (GGS) linker and introduced alanine and charge-reversal mutations to the
416 ^{259}KNxFxKFK^{266} and ^{274}KxRxxKxxKKK^{284} motifs. These mutants were catalytically active and did
417 not affect the ability of LACTB to form filaments, as assessed using negative-stain TEM (S8 Fig).
418 Of note, the flexible loop deletion (ΔL6) and ^{274}ExExxExxEEE^{284} mutant lowered the enzymatic
419 activity of LACTB filaments while the ^{259}EAxAxEAE^{266} mutant displayed increased catalytic activity
420 (S8B Fig). More importantly, the ΔL6 and the ^{259}EAxAxEAE^{266} mutants reduced the membrane
421 tethering ability of LACTB filaments by more than 70% while the ^{274}ExExxExxEEE^{284} mutation led
422 to a ~50% decrease in membrane tethering activity (Fig 5I). We also corroborated these results
423 with computational modeling (S9 Fig). In our cryoEM map, we did not observe clearly resolved
424 densities for the flexible L6 loop region of LACTB. Therefore, we obtained the AlphaFold predicted
425 structure of the human LACTB monomer and calculated the rotational and translation position of
426 the protein in the presence of membranes using the PPM (Positioning of Proteins in Membranes)
427 server (S9 Fig). These theoretical models also nominated the ^{259}KNxFxKFK^{266} motif as key
428 residues involved in membrane tethering, supporting our biochemical findings (S9 Fig). While
429 previous studies claim that this loop may promote self-assembly of the LACTB polymer through
430 a coiled-coil segment [21], we propose that the flexible loop on the fully solvent-exposed exterior
431 of the filament may adopt multiple conformations to accommodate different topologies and
432 curvatures of opposing lipid membranes, thereby mediating protein-lipid interactions that would

433 facilitate membrane organization. Consistent with this, the flexible loop is not conserved amongst
434 the prokaryotic and archaeal PBP-βL family of enzymes, which are not associated with lipid
435 membranes [37], providing additional support for the relevance of this region for membrane
436 binding (S4E Fig). In conclusion, LACTB filaments form stable interactions with cardiolipin-
437 enriched liposomes, display different modes of membrane binding, and the key L6 loop is required
438 for membrane targeting of LACTB filaments.
439
440 **Fig 5. LACTB filaments bind to cardiolipin-enriched liposomes.** (**A-D**) Representative
441 negative-stain TEM images of LACTB filaments in the presence of liposomes. Scale bar, 100 nm.
442 Purified LACTB filaments were incubated with cardiolipin-containing liposomes at room
443 temperature for 4 hours. Red boxes indicate protein-membrane contact sites. (**E**) Zoomed in
444 views of the red boxes in **A**, **B**, **C**, and **D**, showing the details of protein-liposome interactions. (**F**)
445 A schematic diagram of filament-liposome interactions illustrating different membrane binding
446 modes of LACTB filaments. (**G**) Catalytic activity of WT LACTB in the presence of liposomes.
447 Enzyme activity was determined *in vitro* by using a fluorescently labeled substrate and three
448 independent experiments were performed for each sample. Bars represent the mean of at least
449 three independent WT and reconstitution assays. Error bars indicate standard deviation (**H**)
450 Liposome tethering activity of WT LACTB under the presence of liposomes of various
451 compositions. Liposome tethering activity was quantified by counting 1000 filaments from at least
452 three independent reconstitution assays and calculating the total percentage of filament tethering.
453 Bars represent the mean liposome tethering activity and error bars indicate s.e.m. (**I**) Liposome
454 tethering activity of key residues involved in liposome binding. Liposome tethering activity was
455 quantified by counting 1000 filaments from at least three independent reconstitution assays and
456 calculating the total percentage of filament tethering. Bars represent the mean liposome tethering
457 activity of reconstitution assays and error bars indicate s.e.m. Statistical analysis was performed

458 with an unpaired two-tailed Student's t-test (**G**) and unpaired two-tail Welch's t-tests (**H**, **I**). *p
459 <0.05, **p <0.005, ns (no significance). The underlying data in (**G**), (**H**), and (**I**) are provided in
460 sheets Fig 5G, Fig 5H, and Fig 5I in S1 Data.
461
462 **Molecular interpretation of disease-associated mutations.** Given that human LACTB exerts
463 tumor suppression activity in multiple carcinogenic cell lines, we next investigated cancer-specific
464 missense mutations localized within LACTB. We classified LACTB disease mutations in terms of
465 their localization to subunit-subunit interfaces and characterized their effect on the catalytic
466 activity (Fig 6). Currently, over 200 *LACTB* gene variants have been identified, of which ~30% are
467 considered pathogenic [52,53]. About 30% of the pathogenic variants cause frameshifts and
468 premature truncation of the open reading frame, whereas the remaining ~70% are missense
469 mutations that are linked to various cancers [52,53]. Mapping of disease-causing mutations onto
470 our structure of human LACTB demonstrated that some of the pathogenic variants are clustered
471 at the oligomerization interfaces, possibly culminating in a negative effect on filament assembly
472 (Fig 6 and S1 Table). Several mutations related to various types of cancers cluster at the LACTB
473 dimer interface, including V148F, E149Q, E363K, A372T, R371K, K380N, and R382C variants
474 (Fig 6B). Our biochemical characterizations showed that the E149R and R371E charge-reversal
475 mutations resulted in a profound multimerization defect and hindered the catalytic activity of
476 human LACTB (Fig 3C and 3D). Of note, V148, E149, and R371 belong to the L3 loop at the
477 dimerization interface, where E149 and R371 form hydrogen bonds and an inter-molecular salt
478 bridge to stabilize the dimer (Figs 3B and 6B). Moreover, other variants such as R151S, D457K
479 R469K, T472K, R480L, and Y482H, which are located at the polymer filament-forming interfaces,
480 have also been associated with clinical anomalies (Fig 6). As described earlier, we analyzed the
481 assembly properties of the LACTB R151E mutant *in vitro* and found that this mutant depressed
482 the multimerization of human LACTB (Fig 4D-F). Notably, we showed that the disruption of R151-

483 D113 or H352-D457 electrostatic interactions results in a ~60% reduction in the catalytic activity
484 of human LACTB (Fig 4D and 4E). We observed similar results when we assessed the functional
485 role of protruding L15 loop (residues 467 to 482), which contains several disease-associated
486 residues that are critical for filament formation and membrane organization activity of LACTB (Fig
487 4D and 4E). Overall, mutations in these newly evident interfaces would likely have an impact on
488 LACTB polymerization and catalytic activity and this provides important structural context as
489 pathogenic variants in these interfaces are linked to several cancers.
490
491 **Fig 6. The model of LACTB enables mapping the disease-associated mutations.** (**A**) A
492 schematic representation of full-length LACTB architecture. Residues 1-68 contain the predicted
493 mitochondrial targeting sequence (MTS), and residues 243-290 form the flexible loop region.
494 Residues that are associated with various human cancers are highlighted with a red dashed line.
495 (**B**) Ribbon diagram of human LACTB tetramer. Protomers that form the tetramer are labeled A
496 to D and colored as in **Fig 4A**. Mutations localizing to oligomerization interfaces are illustrated as
497 sticks. Inset windows show the close-up views of oligomerization interfaces containing disease-
498 associated mutations. Black boxes indicate the dimer, and polymerization interfaces 1 and 2,
499 respectively.
500
501

502 # Discussion

503 Here, we investigated the molecular mechanism of the LACTB serine protease, whose key
504 functions in mitochondria include the regulation of metabolic pathways and morphology and tumor
505 suppression by modulating mitochondrial lipid metabolism. Our high-resolution structure of the
506 human LACTB filament shows that the enzyme forms a high-order helical filament, which is critical
507 for its cellular function. These results offer new mechanistic insights into how LACTB assembles
508 into filaments to control mitochondrial morphology as well as the efficiency of metabolic
509 processes.

510

511 The basic building block of the helical structure consists of an antiparallel LACTB dimer. This unit
512 then interacts with neighboring homodimers via charge-charge and polar interactions, which
513 results in the helical stacking of LACTB dimers and elongation of filaments (S10 Fig). We show
514 that human LACTB contains novel structural features that are critical for polymerization. Although
515 the active site motifs are conserved between LACTB and the prokaryotic PBP-βL family of
516 enzymes, phylogenetic and structural analyses demonstrate that the residues involved in
517 polymerization are only conserved in higher eukaryotes, suggesting that LACTB has evolved from
518 its prokaryotic counterparts to fulfill different physiological functions in mammals (S5 Fig).
519 Intriguingly, LACTB requires unique contacts to robustly polymerize into filaments which enables
520 catalytic activity. While the benefits of polymeric enzymes are not fully understood, there are
521 several theories of filamentous enzymes exhibiting kinetic advantages. One such kinetic model
522 involves the rapid activation of enzymes through filament formation [54–57]. For instance, the
523 bacterial SgrIR protein, which is a restriction endonuclease, polymerizes rapidly at either end of
524 the filament to stimulate enzyme activity and increase DNA-binding specificity [58,59]. Similarly,
525 many metabolic enzymes such as cytidine triphosphate synthase (CTPS) and inosine
526 monophosphate dehydrogenase (IMPDH) form filaments in bacteria and eukaryotes to modulate

527 enzyme activity [38–41]. Interestingly, CTP-induced polymerization of bacterial CTPS results in
528 decreased catalytic activity, whereas substrate-bound human CTPS filaments display increased
529 enzymatic activity, suggesting that filament formation can tune the activity of metabolic enzymes
530 differently in response to distinct metabolic cues in different species [38]. Additionally, an isoform
531 of human acetyl-CoA carboxylase in the mitochondria forms active and inactive helical filaments
532 through allosteric regulation by citrate and the binding of BRCA1, respectively, revealing a unique
533 form of enzyme regulation via large scale conformational changes in filament architecture [42].
534 The structure of the LACTB filament, together with extensive mutagenesis studies, show that
535 polymerization is essential for the catalytic activity of the enzyme (Fig 3). However, the
536 polymerization interfaces do not participate in active site formation (Fig 4). A possible explanation
537 for this increased enzymatic activity upon filament assembly is that the binding of LACTB
538 protomers indirectly stabilizes the regions involved in substrate binding and thus enhances the
539 catalytic activity of LACTB. The stabilization of the LACTB filament through multiple intra- and
540 inter-dimeric interfaces that are largely mediated by charged and polar interactions strongly
541 suggest that the filament assembly is responsible for the observed amplification of LACTB activity
542 in our biochemical data. Our results suggest that the catalytic activity of human LACTB is
543 allosterically regulated by stabilizing an intrinsically inactive state upon filament formation,
544 independent of substrate binding, thus holding the enzyme in an active conformation.
545 Filamentation appears to be an evolutionarily conserved mechanism in a diverse array of
546 biochemical and biological pathways in cells and provides an added layer of regulation in the form
547 of rapid activation or inhibition [56,60]. By characterizing distinct interactions in LACTB filaments
548 our data provides a structural basis for manipulating LACTB polymerization *in vivo*.
549
550 Many different enzymes dynamically form filaments in response to changing physiological
551 conditions in cells [38,41,42,44,61]. The process of polymerization requires a critical

552 concentration of monomeric protein for filament formation, where larger self-assemblies can be
553 formed as a result of protein crowding [56]. In addition to modulating enzyme activity through
554 polymerization, an unexpected feature of the LACTB filaments is their ability to interact with lipid
555 membranes. Our results indicate that both LACTB-mediated mitochondrial membrane
556 organization and regulation of lipid metabolism may be directly linked to its ability to form higher-
557 order assemblies. However, it is not clear whether the catalytic activity of LACTB plays a role in
558 membrane organization in mitochondria as its direct substrate remains unknown. Unlike many
559 membrane-associated proteins such as conserved septin proteins in mammals [62], membrane
560 binding does not influence LACTB polymerization through the end-to-end association of the
561 homodimers. It is striking that while many regulatory enzymes polymerize to allosterically tune
562 enzyme kinetics [56], LACTB exerts a dual function and forms exclusively cooperative filaments
563 to interact with mitochondrial membranes from the inside. We showed that the LACTB filaments
564 are unique as they contain specific sequences to interact directly with membranes (Fig 5). The
565 membrane topologies observed in electron tomograms of mitochondria suggest that LACTB
566 filaments, which have the ability to access length scales larger than the size of mitochondrial
567 membrane compartments, can form structural and functional bridges between mitochondrial IM
568 and OM and regulate the distance between the opposing faces of the cristae membrane [63].
569 Hence, LACTB assemblies may have further roles in mitochondrial morphogenesis and in
570 processes, where strong membrane association is needed. Mitochondrial membranes have a
571 unique lipid composition that is important for the organelle's morphology and proper function of
572 membrane-associated processes [7]. In addition to the major phospholipids PE and PC, which
573 account for a large portion of mitochondrial membrane lipids, mitochondria-exclusive phospholipid
574 cardiolipin (CL) is a distinguishing component of the mitochondrial IM that is known to participate
575 in a wide range of mitochondrial processes [10]. CL directly interacts with positively charged
576 surfaces of numerous mitochondrial proteins with its negatively charged headgroup and

577 contributes to the dynamic membrane organization in mitochondria [64,65]. Negative-stain TEM
578 imaging revealed that LACTB filaments have a high affinity for cardiolipin-containing lipid bilayers
579 and manifest two different membrane binding modes (Fig 5). We postulate that LACTB filaments
580 are recruited to the inner/outer membrane by electrostatic interactions between negatively
581 charged phospholipids and the flexible polybasic surface loop of LACTB. When the tip of the
582 LACTB filaments binds lipid membranes, subunits of adjacent homodimers form additional
583 protein-lipid interactions through lateral associations, increasing the filament contacts with the
584 membrane surface. Furthermore, subunits on the opposite end of the filament bind membranes
585 in a similar fashion and engage in lateral associations via interactions of several subunits, thus
586 bringing the two membranes into close apposition. We, therefore, propose that upon forming
587 filaments between the two membranes, human LACTB can act as a molecular zipper and regulate
588 mitochondrial membrane organization by controlling the distance between the two membranes.
589 LACTB filaments display a strong driving force for the spatial arrangement of membranes, thus
590 providing a structural foundation for a wide variety of normal and pathological processes.
591
592 Finally, our ability to map mutations that are identified in various cancers to the LACTB structure
593 expands the breadth of deficiency mechanisms (beyond the downregulation of LACTB by several
594 miRNAs) to additionally include the impaired ability of LACTB to correctly assemble into a
595 filament. Our structural model encompasses nearly all human cancer-associated missense
596 mutations in LACTB and lays the foundation for characterizing additional mechanisms leading to
597 LACTB perturbation in the regulation of lipid metabolism and mitochondrial membrane
598 organization. This study uncovers an important aspect of how LACTB functions as a tumor
599 suppressor and provides a foundation for future cancer research and drug therapy with LACTB
600 as a target.
601

602 While this manuscript was under preparation, Zhang *et al.* determined the single-particle cryoEM
603 structure of the LACTB and studied the catalytic activity of the enzyme [66]. Using topology-
604 independent structure comparison, we determined 98.74% alignment and a root mean square
605 deviation (r.m.s.d.) of 0.48 Å over 389 Cα atoms between the two monomeric structures. Although
606 the overall structure of the monomeric enzyme is similar, Zhang *et al.* studied smaller LACTB
607 oligomers that do not form elongated filaments. Our cryoEM structure of LACTB filament mirrors
608 data that were previously obtained *in situ* [21], emphasizing that structure determination of self-
609 assembled micron-scale filaments generates biologically relevant atomic models. Overall, our
610 structural models and biochemical characterizations of assembly interfaces largely agree with the
611 recently published study [66]. Moreover, our results on the assembly mechanism of LACTB and
612 several other structural and functional analyses, including the details of protein-lipid interactions,
613 which are critical for characterizing the regulatory role of a filamentous enzyme, provide an
614 important basis for the elucidation of the mechanisms of LACTB protease on a molecular level.
615

616 # Materials and Methods

617 **Protein expression and purification**

618 The gene encoding human LACTB (residues 1-547) was obtained from DNASU
619 (HsCD00629745). The DNA sequence for human LACTB (residues 97-547) was subcloned into
620 the multiple cloning site of the pCA528 bacterial expression vector. LACTB was tagged with an
621 N-terminal 6x-His tag followed by a SUMO tag. All mutant constructs were generated by a two-
622 step site-directed mutagenesis PCR protocol. The plasmid was transformed into *Escherichia coli*
623 BL21(DE3)-RIPL cells and expressed in ZYP-5052 auto-induction media at 18°C for 16 h when
624 OD_{600} reached 0.6-0.8. Cells were harvested with centrifugation (Sorvall RC-5B Superspeed
625 Centrifuge) at 10,800 rpm (39,531x *g*) for 20 min at 4 °C. The supernatant was then discarded,
626 and the cell pellets were resuspended in lysis buffer (50 mM HEPES-NaOH, pH 7.5, 500 mM
627 NaCl, 5 mM $MgCl_2$, 20 mM imidazole, 1mM CHAPS (Anatrace), 5mM 2-mercaptoethanol, 10%
628 (v/v) glycerol) supplemented with 0.5% (v/v) Triton X-100, 0.5 mg DNase I, and 1X EDTA-free
629 complete protease inhibitor cocktail (Roche). The cells were lysed with an Emusliflex C3
630 Homogenizer and the cell lysate was clarified by centrifugation (Sorvall RC-5B Superspeed
631 Centrifuge) at 15,000 rpm (68,040x *g*) at 4 °C for 45 min. The supernatant was incubated with Ni-
632 NTA agarose beads (Qiagen) for 1 h. The Ni-NTA beads were washed with 20 column volumes
633 (CV) of lysis buffer, 10 CV of wash buffer (50 mM HEPES-NaOH, pH 7.5, 1M NaCl, 5 mM $MgCl_2$,
634 20 mM imidazole, 1mM CHAPS, 5mM 2-mercaptoethanol, 10% (v/v) glycerol), and 10 CV of lysis
635 buffer again before the protein was eluted with 5 CV elution buffer (50 mM HEPES-NaOH, pH
636 7.5, 500 mM NaCl, 5 mM $MgCl_2$, 500 mM imidazole, 1mM CHAPS, 5mM 2-mercaptoethanol, and
637 10% (v/v) glycerol). The sample was then dialyzed into lysis buffer containing Ulp1 protease to
638 remove the N-terminal 6x-His-SUMO tag overnight at 4 °C. The dialyzed protein was concentrated
639 using a 30 kDa MWCO concentrator (Millipore) and was further purified by size-exclusion
640 chromatography on a Superose 6 Increase 10/300 GL column (Cytiva) equilibrated with

641 purification buffer (20 mM HEPES-NaOH, pH 7.5, 140 mM NaCl, 10 mM KCl, 1mM $MgCl_2$, and 1
642 mM DTT). A typical size-exclusion profile for WT LACTB consisted of a large peak containing
643 LACTB filaments eluting within the void volume (V_0) of the column. Fractions of LACTB were
644 analyzed by SDS-PAGE. Freshly purified samples were used for cryoEM grid preparation and *in*
645 *vitro* substrate binding assays.
646
647 **Negative-stain electron microscopy**
648 The LACTB assembly was purified as described above. Size-exclusion peak fractions
649 corresponding to LACTB were diluted to ~2.0 μM for negative-stain transmission electron
650 microscope (TEM). Samples were prepared by applying 4 μl of purified LACTB applied onto glow-
651 discharged carbon-coated copper grids (400 mesh) and negatively stained with 0.75% (w/v)
652 uranyl formate (UF) following an established protocol [67]. Briefly, the samples were incubated
653 on the grid for 1 min and then blotted off with filter paper. Subsequently, samples on grids were
654 stained with UF for 45 s and air dried for 2 min at room temperature. The grids were imaged using
655 a Tecnai T12 Spirit LaB6 filament TEM (FEI) equipped with an AMT 2k x 2k side-mounted CCD
656 camera and operated at a voltage of 100 kV. The micrographs were collected at a nominal
657 magnification of 120,000x at the specimen level with a calibrated pixel size of 5.28 Å per pixel.
658
659 **CryoEM sample preparation and data acquisition**
660 Prior to cryoEM grid preparation, an aliquot of purified LACTB was buffer exchanged to a freezing
661 buffer (20 mM HEPES-NaOH, pH 7.5, 140 mM NaCl, 10 mM KCl, 1 mM $MgCl_2$, 1mM DTT, 1%
662 glycerol, and 1 mM CHAPS) by centrifugation at 1000x *g* for 2 minutes with a micro-spin desalting
663 column (Thermo Scientific Zeba) at 4 °C. Aliquots of 4 μl of protein samples (0.3 mg ml^{-1} or ~6
664 μM) were applied to glow-discharged R1.2/1.3 200 Cu mesh grids (Quantifoil). After 30 s, the
665 grids were blotted for 3 seconds and plunged into liquid ethane using a Leica EM GP2 Automatic

666 Plunge Freezer operated at 10 °C and 90% humidity. Micrographs were acquired using a Titan
667 Krios TEM (FEI) operated at 300 kV and equipped with a K3 Summit direct electron detector
668 (Gatan). Images of frozen-hydrated filaments of LACTB were collected in counting mode at a
669 nominal magnification of 29,000x corresponding to an image pixel size of 0.8211 Å on the
670 specimen level, applying a defocus range of -0.5 to -1.5 µm. A total of 7643 dose-fractionated
671 movies were recorded with the SerialEM software [68] multishot method over nine neighboring
672 holes (3 x 3). The dose rate was 1.05 electrons/$Å^2$/frame, with a frame rate of 0.07 s, resulting in
673 a total exposure time of 3.985 s and a total accumulated dose of 59.58 electrons per $Å^2$ (57
674 frames). CryoEM data collection parameters are summarized in Table 1.
675
676 **Image analysis and 3D reconstruction**
677 The alignment and dose-weighted summation of raw movie stacks were carried out using
678 MotionCor2 [69]. Contrast transfer function (CTF) estimations were performed on aligned, non-
679 dose-weighted micrographs using CTFFIND4 [70]. All subsequent processing steps were
680 performed using Relion 3.1 [71,72]. A total of 34,636 filament coordinates were manually picked
681 and filament segments with 90% overlap were extracted by using a box size of 320 pixels. All
682 segments (430,592) were then subjected to multiple rounds of reference-free two-dimensional
683 (2D) classification with 100 classes to identify structurally homogeneous subsets. After 2D
684 classification, a featureless cylinder-shaped electron density map with a 160 nm diameter was
685 generated in Relion and used as an initial reference for 3D auto-refinement with C1 symmetry.
686 The resulting refined map showed clear secondary structure features and was used to estimate
687 the helical parameters. Using this 4.3 Å reconstruction, an initial 3D classification was performed
688 with C1 symmetry, and the segments from the best 3D classes (248,548 segments) were selected
689 for high-resolution 3D auto-refinement. Subsequently, these segments were 3D auto-refined with
690 a soft mask, central Z length of 45% of the box size (helical_z_percentage=0.45), and imposing

691 starting helical parameters of 21.59 Å rise and 48.91° twist, yielding a 3D reconstruction with an
692 overall resolution of 3.7 Å. To improve this density map, the final particle segments were subjected
693 to iterative rounds of focused 3D auto-refinement, CTF refinement, and Bayesian polishing to
694 obtain a final 3D reconstruction of a right-handed helical assembly at 3.1 Å resolution. The helical
695 parameters converged to a rise of 21.63 Å and a twist of 48.25° per subunit. A reconstruction
696 without imposing symmetry was also generated at 3.1 Å resolution after focus refinement using a
697 similar mask on the filament. The final reported resolutions are based on the gold-standard
698 Fourier shell correlation (FSC) = 0.143 criterion. Maps were sharpened by applying a negative *B*
699 factor as determined by the Relion post-processing program. The local resolution estimation was
700 calculated by ResMap using half-map reconstructions [73].
701
702 **Model building and refinement**
703 Model building was carried out using the 3.1 Å cryoEM map of the human LACTB filament. The
704 Alphafold [74] predicted structure of monomeric LACTB was used as an initial model for atomic
705 model building. The model was manually fitted into the cryoEM density map using UCSF Chimera
706 [75] and then rigid body refined using the real-space refinement procedure implemented in the
707 program PHENIX [76]. Atomic coordinates of the human LACTB (residues 97-547) filament were
708 manually rebuilt using the program Coot [77] and the final models were iteratively refined against
709 the cryoEM density map. The real space-refinement of models with global minimization, local grid
710 search, secondary structure, and geometric restraints applied was performed using the software
711 PHENIX [76]. Secondary structure elements and side chains for the majority of the residues were
712 unambiguously resolved. Each residue was manually inspected, and correction of the refined
713 coordinates was performed by applying torsion, planar peptide, and Ramachandran restraints
714 during manual rebuilding in Coot [77].
715

716 **Validation and structural analysis**

717 The stereochemistry and geometry of the final model was evaluated by MolProbity [78]. CryoEM
718 maps and atomic models were analyzed, and figures were generated using UCSF ChimeraX [79],
719 UCSF Chimera [75], and PyMOL (The PyMOL Molecular Graphics System, Version 2.0
720 Schrödinger, LLC). Negative-stain TEM images were analyzed using FIJI [80]. Surface potential
721 renderings were generated using the APBS plugin in PyMOL [81]. Structural and chemical
722 properties of macromolecular interfaces and surfaces were analyzed by the PISA server [82]. The
723 fold conservation analysis was performed with the Dali server [83] and structural comparisons to
724 the PBP-βL family of enzymes and RMSD calculations were carried out using the CLICK server
725 [84]. Sequence alignment of the LACTB homologs as well as the PBP-βL family of enzymes was
726 generated using Clustal Omega [85] and sequence conservation figures were prepared by using
727 the Clustal Omega alignment file and LACTB model in ESPript server 3.0 [86]. Schematic
728 diagrams were generated by using BioRender.com. The statistics of the cryoEM helical
729 reconstruction and model refinement were summarized in Table 1.

730

731 **LACTB *in vitro* substrate assay**

732 To determine the catalytic activity of the WT and mutant LACTB, the cleavage of the fluorogenic
733 Ac-YVAD-AMC peptide (Enzo Life Sciences) was measured at an excitation wavelength of 380
734 nm and an emission wavelength of 460 nm using a CLARIOstar microplate reader. All assays
735 were performed at room temperature and the total reaction volumes were 20 µl. Briefly, 10 µl of
736 purified LACTB protein was mixed with a reaction buffer containing 20 mM HEPES-NaOH, pH
737 7.5, 140 mM NaCl, 10 mM KCl, 1 mM $MgCl_2$, 1 mM DTT, and 0.01% NP-40 detergent
738 (AmericanBio) to generate a final protein concentration of 12-15 nM. Reactions were initiated by
739 adding 100 µM concentrations of the substrate Ac-YVAD-AMC (dissolved in DMSO and prediluted
740 to 200 µM in reaction buffer) to the enzyme in a 384 well black polystyrene assay plate (Costar

741 3916). The reactions were run in at least three independent replicates for 1,200 s and
742 fluorescence was measured every 10 s. The raw data were averaged to determine reaction rates
743 from the linear part of the curve and include standard deviation. To determine the catalytic activity
744 of the WT LACTB in the presence of lipid vesicles, freshly purified protein (1.5-2 μM) was
745 incubated with 0.5 mg ml^{-1} unilamellar liposomes in three independent experiments for 4 h at room
746 temperature. Then, the catalytic activity of LACTB was measured as described above to quantify
747 the reaction rate of WT LACTB in the presence of liposomes.
748
749 **H_2O_2 treatment of LACTB filaments**
750 An aliquot of purified LACTB was diluted to 0.15 mg ml^{-1}. Aliquots of 10 μl of the protein sample
751 were incubated with 5 μl of varying concentrations of H_2O_2 for 30 minutes. The final concentrations
752 were 0.01% H_2O_2 (v/v), 0.025%, 0.05%, 0.1%, 0.25%, 0.5%, 0.75%, and 1.0%. The final
753 concentration of protein was 0.1 mg ml^{-1}. The samples were analyzed by SDS PAGE using a 4-
754 15% precast gel (BioRad) at 100 V. The 0.1%, 0.5%, and 1.0% H_2O_2 (v/v) samples were stained
755 on glow-discharged carbon-coated copper grids with UF as described above and visualized with
756 a Tecnai T12 Spirit TEM (FEI) operated at a voltage of 100 kV. The micrographs were collected
757 at a nominal magnification of 120,000x at the specimen level with a calibrated pixel size of 5.28
758 Å per pixel.
759
760 **Preparation of lipid vesicles and LACTB membrane binding reactions**
761 To determine the membrane binding activity of human LACTB, the lipid composition of the
762 mitochondrial inner membrane was used to prepare vesicles as described previously [87]. The
763 lipid stock solutions were resuspended in chloroform, methanol, and water mixture (20:9:1, (v/v/v))
764 and stored at -20°C. 1-palmitoyl-2-oleoyl-glycero-3-phosphocholine (POPC), 1-palmitoyl-2-
765 oleoyl-sn-glycero-3-phosphoethanolamine (POPE), L-α-lysophosphatidylinositol (Soy Lyso PI),

766 1',3'-bis[1,2-dioleoyl-sn-glycero-3-phospho]-glycerol (cardiolipin $(18:1)_4$), D-galactosyl-ß-1,1' N-
767 nervonoyl-D-erythro-sphingosine (C24:1 Galactosyl(ß) Ceramide, GalCer) (Avanti Polar Lipids)
768 were mixed in a molar ratio of POPC:POPE:PI:CL; 45:22:8:25, POPC:POPE:PI; 70:22:8,
769 POPC:POPE; 78:22, POPC; 100, and GalCer:CL; 80:20. The lipid mixture was then dried as a
770 thin film in a glass tube under a gentle stream of nitrogen and incubated in a vacuum desiccator
771 for 4 h to remove excess solvent. Following dehydration, the lipid film was resuspended for 30
772 min at room temperature in a liposome buffer containing 20mM HEPES-NaOH, pH 7.5, and
773 150mM NaCl. The suspension was extruded through polycarbonate membranes with a 50 nm
774 pore diameter using Avanti Mini Extruder (Avanti Polar Lipids) to obtain unilamellar liposomes. 20
775 µl aliquots of rehydrated lipids were flash-frozen in liquid nitrogen and stored at -80°C. The
776 nanotube mixtures were rehydrated in liposome buffer and incubated at room temperature for 15
777 min with intermittent mixing. The suspended mixture of lipid nanotubes was briefly vortexed and
778 sonicated for three rounds (5 min per round) in a bath sonicator at 50°C. The lipids were
779 immediately used in the binding assays after cooling at room temperature.
780
781 For liposome binding assays, a range of 1.5-2 µM of freshly purified WT LACTB was incubated
782 with 0.5 mg ml^{-1} unilamellar liposomes or the liposome reaction buffer (20 mM HEPES-NaOH, pH
783 7.5, 140 mM NaCl, 10 mM KCl, 1 mM $MgCl_2$, 1 mM DTT) for 4 h at room temperature.
784 Subsequently, the reaction mixture was applied onto glow-discharged carbon-coated copper grids
785 and negatively stained with UF. The membrane binding activity of LACTB filaments was assessed
786 by negative-stain TEM. Images were collected using a Tecnai T12 Spirit TEM (FEI) equipped with
787 an AMT 2k x 2k side-mounted CCD camera as described above. Negative stain images were
788 recorded at a nominal magnification of 120,000x at the specimen level with a calibrated pixel size
789 of 5.28 Å per pixel. A total of 1000 filaments were counted from randomized blinded images to

790 eliminate bias. The total percentage of filaments interacting with one or more liposomes (binding
791 and tethering, respectively) was determined and the s.e.m. for each sample was calculated.
792
793 **Statistical analysis**
794 Statistical significance was determined using GraphPad Prism 9 software. Liposome tethering
795 experiments and related enzymatic activity measurements were analyzed by unpaired two-tailed
796 Welch's t-test and unpaired two-tailed Student's t-test, respectively. The values $P < 0.05$ were
797 considered statistically significant.
798
799 **Data Accessibility**
800 All of the 3D cryoEM data that support the findings of this study have been deposited in Electron
801 Microscopy Data Bank with the accession code: EMDB-26595. The model coordinates have been
802 deposited in the Protein Data Bank under accession code PDB ID: 7ULW.
803

Acknowledgments

We thank the current members of the Aydin laboratory for helpful discussions and assistance on this project. We especially thank Charles Moe at the BioChemistry Krios Electron Microscopy (BioKEM) Facility of the University of Colorado Boulder for his support with data collection and EM infrastructure; Garry Morgan and Courtney Ozzello at the EM Services Core Facility of the University of Colorado Boulder for electron microscopy training and support; the Shared Instrument Pool (SIP) core facility (RRID: SCR_018986) of the Department of Biochemistry at the University of Colorado Boulder for the use of the shared research instrumentation infrastructure; Dr. Annette Erbse for assistance with biophysical instruments and support; Dr. Chris Ebmeier and the Mass Spectrometry Core Facility of the University of Colorado Boulder, which is supported by NIH Grants S10OD025267 and S10RR026641 grants, for mass spectrometry analysis; Dr. Kelly Zuccaro for assistance with computer infrastructure and liposome preparation. We also thank Professor Karolin Luger for her support and for kindly sharing the equipment for the fluorescence-based activity assays. The results shown here are in part based upon data generated by the TCGA Research Network: https://www.cancer.gov/tcga.

Competing interests

The authors declare no competing interests.

Correspondence and requests for materials should be addressed to H.A.

825 ## References

826 1. Mottis A, Herzig S, Auwerx J. Mitocellular communication: Shaping health and disease.
827 Science. 2019;366: 827–832. doi:10.1126/science.aax3768

828 2. Spinelli JB, Haigis MC. The multifaceted contributions of mitochondria to cellular
829 metabolism. Nat Cell Biol. 2018;20: 745–754. doi:10.1038/s41556-018-0124-1

830 3. Iovine JC, Claypool SM, Alder NN. Mitochondrial compartmentalization: emerging themes in
831 structure and function. Trends Biochem Sci. 2021;46: 902–917.
832 doi:10.1016/j.tibs.2021.06.003

833 4. Friedman JR, Nunnari J. Mitochondrial form and function. Nature. 2014;505: 335–343.
834 doi:10.1038/nature12985

835 5. Chan DC. Mitochondrial Dynamics and Its Involvement in Disease. Annu Rev Pathol Mech
836 Dis. 2020;15: 235–259. doi:10.1146/annurev-pathmechdis-012419-032711

837 6. Eisner V, Picard M, Hajnóczky G. Mitochondrial dynamics in adaptive and maladaptive
838 cellular stress responses. Nat Cell Biol. 2018;20: 755–765. doi:10.1038/s41556-018-0133-
839 0

840 7. Mayr JA. Lipid metabolism in mitochondrial membranes. J Inherit Metab Dis. 2015;38: 137–
841 144. doi:10.1007/s10545-014-9748-x

842 8. Stefely JA, Pagliarini DJ. Biochemistry of Mitochondrial Coenzyme Q Biosynthesis. Trends
843 Biochem Sci. 2017;42: 824–843. doi:10.1016/j.tibs.2017.06.008

844 9. Manicki M, Aydin H, Abriata LA, Overmyer KA, Guerra RM, Coon JJ, et al. Structure and
845 functionality of a multimeric human COQ7:COQ9 complex. Mol Cell 2022;82: 1–17.
846 doi:10.1016/j.molcel.2022.10.003

847 10. Mårtensson CU, Doan KN, Becker T. Effects of lipids on mitochondrial functions. Biochim
848 Biophys Acta BBA - Mol Cell Biol Lipids. 2017;1862: 102–113.
849 doi:10.1016/j.bbalip.2016.06.015

850 11. Basu Ball W, Neff JK, Gohil VM. The role of nonbilayer phospholipids in mitochondrial
851 structure and function. FEBS Lett. 2018;592: 1273–1290. doi:10.1002/1873-3468.12887

852 12. Steenbergen R, Nanowski TS, Beigneux A, Kulinski A, Young SG, Vance JE. Disruption of
853 the Phosphatidylserine Decarboxylase Gene in Mice Causes Embryonic Lethality and
854 Mitochondrial Defects. J Biol Chem. 2005;280: 40032–40040. doi:10.1074/jbc.M506510200

855 13. Calzada E, Avery E, Sam PN, Modak A, Wang C, McCaffery JM, et al.
856 Phosphatidylethanolamine made in the inner mitochondrial membrane is essential for yeast
857 cytochrome bc1 complex function. Nat Commun. 2019;10: 1432. doi:10.1038/s41467-019-
858 09425-1

859 14. Tasseva G, Bai HD, Davidescu M, Haromy A, Michelakis E, Vance JE.
860 Phosphatidylethanolamine Deficiency in Mammalian Mitochondria Impairs Oxidative

861 Phosphorylation and Alters Mitochondrial Morphology. J Biol Chem. 2013;288: 4158–4173.
862 doi:10.1074/jbc.M112.434183

863 15. Snaebjornsson MT, Janaki-Raman S, Schulze A. Greasing the Wheels of the Cancer
864 Machine: The Role of Lipid Metabolism in Cancer. Cell Metab. 2020;31: 62–76.
865 doi:10.1016/j.cmet.2019.11.010

866 16. Vyas S, Zaganjor E, Haigis MC. Mitochondria and Cancer. Cell. 2016;166: 555–566.
867 doi:10.1016/j.cell.2016.07.002

868 17. Porporato PE, Filigheddu N, Pedro JMB-S, Kroemer G, Galluzzi L. Mitochondrial metabolism
869 and cancer. Cell Res. 2018;28: 265–280. doi:10.1038/cr.2017.155

870 18. Bar-Peled L, Chantranupong L, Cherniack AD, Chen WW, Ottina KA, Grabiner BC, et al. A
871 Tumor Suppressor Complex with GAP Activity for the Rag GTPases That Signal Amino Acid
872 Sufficiency to mTORC1. Science. 2013;340: 1100–1106. doi:10.1126/science.1232044

873 19. Chaker-Margot M, Werten S, Dunzendorfer-Matt T, Lechner S, Ruepp A, Scheffzek K, et al.
874 Structural basis of activation of the tumor suppressor protein neurofibromin. Mol Cell.
875 2022;82: 1288-1296.e5. doi:10.1016/j.molcel.2022.03.011

876 20. Keckesova Z, Donaher JL, De Cock J, Freinkman E, Lingrell S, Bachovchin DA, et al. LACTB
877 is a tumour suppressor that modulates lipid metabolism and cell state. Nature. 2017;543:
878 681–686. doi:10.1038/nature21408

879 21. Polianskyte Z, Peitsaro N, Dapkunas A, Liobikas J, Soliymani R, Lalowski M, et al. LACTB
880 is a filament-forming protein localized in mitochondria. Proc Natl Acad Sci. 2009;106: 18960–
881 18965. doi:10.1073/pnas.0906734106

882 22. Hung V, Zou P, Rhee H-W, Udeshi ND, Cracan V, Svinkina T, et al. Proteomic Mapping of
883 the Human Mitochondrial Intermembrane Space in Live Cells via Ratiometric APEX Tagging.
884 Mol Cell. 2014;55: 332–341. doi:10.1016/j.molcel.2014.06.003

885 23. Smith TS, Southan C, Ellington K, Campbell D, Tew DG, Debouck C. Identification, Genomic
886 Organization, and mRNA Expression of LACTB, Encoding a Serine β-Lactamase-like
887 Protein with an Amino-terminal Transmembrane Domain. Genomics. 2001;78: 12–14.
888 doi:10.1006/geno.2001.6643

889 24. Ma Y, Wang L, He F, Yang J, Ding Y, Ge S, et al. LACTB suppresses melanoma progression
890 by attenuating PP1A and YAP interaction. Cancer Lett. 2021;506: 67–82.
891 doi:10.1016/j.canlet.2021.02.022

892 25. Xu W, Yu M, Qin J, Luo Y, Zhong M. LACTB Regulates PIK3R3 to Promote Autophagy and
893 Inhibit EMT and Proliferation Through the PI3K/AKT/mTOR Signaling Pathway in Colorectal
894 Cancer. Cancer Manag Res. 2020;Volume 12: 5181–5200. doi:10.2147/CMAR.S250661

895 26. Li H-T, Dong D-Y, Liu Q, Xu Y-Q, Chen L. Overexpression of LACTB, a Mitochondrial Protein
896 That Inhibits Proliferation and Invasion in Glioma Cells. Oncol Res Featur Preclin Clin
897 Cancer Ther. 2019;27: 423–429. doi:10.3727/096504017X15030178624579

898 27. Zeng K, Chen X, Hu X, Liu X, Xu T, Sun H, et al. LACTB, a novel epigenetic silenced tumor
899 suppressor, inhibits colorectal cancer progression by attenuating MDM2-mediated p53
900 ubiquitination and degradation. Oncogene. 2018;37: 5534–5551. doi:10.1038/s41388-018-
901 0352-7

902 28. Zhang J, He Y, Yu Y, Chen X, Cui G, Wang W, et al. Upregulation of miR-374a promotes
903 tumor metastasis and progression by downregulating LACTB and predicts unfavorable
904 prognosis in breast cancer. Cancer Med. 2018;7: 3351–3362. doi:10.1002/cam4.1576

905 29. Liu J, Yang L, Yuan X, Xiong M, Zhu J, Wu W, et al. Targeted Nanotherapeutics Using
906 LACTB Gene Therapy Against Melanoma. Int J Nanomedicine. 2021;Volume 16: 7697–
907 7709. doi:10.2147/IJN.S331519

908 30. Eriksson O, Lalowski M, Lindholm D. Commentary: LACTB is a tumour suppressor that
909 modulates lipid metabolism and cell state. Front Physiol. 2017;8: 396.
910 doi:10.3389/fphys.2017.00396

911 31. Chan EYL, McQuibban GA. Phosphatidylserine Decarboxylase 1 (Psd1) Promotes
912 Mitochondrial Fusion by Regulating the Biophysical Properties of the Mitochondrial
913 Membrane and Alternative Topogenesis of Mitochondrial Genome Maintenance Protein 1
914 (Mgm1). J Biol Chem. 2012;287: 40131–40139. doi:10.1074/jbc.M112.399428

915 32. Frohman MA. Role of mitochondrial lipids in guiding fission and fusion. J Mol Med. 2015;93:
916 263–269. doi:10.1007/s00109-014-1237-z

917 33. Pagliarini DJ, Calvo SE, Chang B, Sheth SA, Vafai SB, Ong S-E, et al. A Mitochondrial
918 Protein Compendium Elucidates Complex I Disease Biology. Cell. 2008;134: 112–123.
919 doi:10.1016/j.cell.2008.06.016

920 34. Chen Y, Zhu J, Lum PY, Yang X, Pinto S, MacNeil DJ, et al. Variations in DNA elucidate
921 molecular networks that cause disease. Nature. 2008;452: 429–435.
922 doi:10.1038/nature06757

923 35. Yang X, Deignan JL, Qi H, Zhu J, Qian S, Zhong J, et al. Validation of candidate causal
924 genes for obesity that affect shared metabolic pathways and networks. Nat Genet. 2009;41:
925 415–423. doi:10.1038/ng.325

926 36. Gonzalez-Franquesa A, Stocks B, Chubanava S, Hattel HB, Moreno-Justicia R, Peijs L, et
927 al. Mass-spectrometry-based proteomics reveals mitochondrial supercomplexome plasticity.
928 Cell Rep. 2021;35: 109180. doi:10.1016/j.celrep.2021.109180

929 37. Peitsaro N, Polianskyte Z, Tuimala J, Pörn-Ares I, Liobikas J, Speer O, et al. Evolution of a
930 family of metazoan active-site-serine enzymes from penicillin-binding proteins: a novel facet
931 of the bacterial legacy. BMC Evol Biol. 2008;8: 26. doi:10.1186/1471-2148-8-26

932 38. Lynch EM, Hicks DR, Shepherd M, Endrizzi JA, Maker A, Hansen JM, et al. Human CTP
933 synthase filament structure reveals the active enzyme conformation. Nat Struct Mol Biol.
934 2017;24: 507–514. doi:10.1038/nsmb.3407

935 39. Lynch EM, Kollman JM. Coupled structural transitions enable highly cooperative regulation
936 of human CTPS2 filaments. Nat Struct Mol Biol. 2020;27: 42–48. doi:10.1038/s41594-019-
937 0352-5

938 40. Lynch EM, DiMattia MA, Albanese S, van Zundert GCP, Hansen JM, Quispe JD, et al.
939 Structural basis for isoform-specific inhibition of human CTPS1. Proc Natl Acad Sci.
940 2021;118: e2107968118. doi:10.1073/pnas.2107968118

941 41. Johnson MC, Kollman JM. Cryo-EM structures demonstrate human IMPDH2 filament
942 assembly tunes allosteric regulation. eLife. 2020;9: e53243. doi:10.7554/eLife.53243

943 42. Hunkeler M, Hagmann A, Stuttfeld E, Chami M, Guri Y, Stahlberg H, et al. Structural basis
944 for regulation of human acetyl-CoA carboxylase. Nature. 2018;558: 470–474.
945 doi:10.1038/s41586-018-0201-4

946 43. Kim G, Azmi L, Jang S, Jung T, Hebert H, Roe AJ, et al. Aldehyde-alcohol dehydrogenase
947 forms a high-order spirosome architecture critical for its activity. Nat Commun. 2019;10:
948 4527. doi:10.1038/s41467-019-12427-8

949 44. Webb BA, Dosey AM, Wittmann T, Kollman JM, Barber DL. The glycolytic enzyme
950 phosphofructokinase-1 assembles into filaments. J Cell Biol. 2017;216: 2305–2313.
951 doi:10.1083/jcb.201701084

952 45. Petrovska I, Nüske E, Munder MC, Kulasegaran G, Malinovska L, Kroschwald S, et al.
953 Filament formation by metabolic enzymes is a specific adaptation to an advanced state of
954 cellular starvation. eLife. 2014;3: e02409. doi:10.7554/eLife.02409

955 46. Sena LA, Chandel NS. Physiological Roles of Mitochondrial Reactive Oxygen Species. Mol
956 Cell. 2012;48: 158–167. doi:10.1016/j.molcel.2012.09.025

957 47. Auten RL, Davis JM. Oxygen Toxicity and Reactive Oxygen Species: The Devil Is in the
958 Details. Pediatr Res. 2009;66: 121–127. doi:10.1203/PDR.0b013e3181a9eafb

959 48. DalleDonne I, Milzani A, Colombo R. H2O2-treated actin: assembly and polymer interactions
960 with cross-linking proteins. Biophys J. 1995;69: 2710–2719. doi:10.1016/S0006-
961 3495(95)80142-6

962 49. Shutt T, Geoffrion M, Milne R, McBride HM. The intracellular redox state is a core
963 determinant of mitochondrial fusion. EMBO Rep. 2012;13: 909–915.
964 doi:10.1038/embor.2012.128

965 50. Norton M, Ng AC-H, Baird S, Dumoulin A, Shutt T, Mah N, et al. ROMO1 Is an Essential
966 Redox-Dependent Regulator of Mitochondrial Dynamics. Sci Signal. 2014;7: ra10–ra10.
967 doi:10.1126/scisignal.2004374

968 51. Brambley CA, Marsee JD, Halper N, Miller JM. Characterization of Mitochondrial YME1L
969 Protease Oxidative Stress-Induced Conformational State. J Mol Biol. 2019;431: 1250–1266.
970 doi:10.1016/j.jmb.2019.01.039

971 52. Karczewski KJ, Francioli LC, Tiao G, Cummings BB, Alföldi J, Wang Q, et al. The mutational
972 constraint spectrum quantified from variation in 141,456 humans. Nature. 2020;581: 434–
973 443. doi:10.1038/s41586-020-2308-7

974 53. Tate JG, Bamford S, Jubb HC, Sondka Z, Beare DM, Bindal N, et al. COSMIC: the Catalogue
975 Of Somatic Mutations In Cancer. Nucleic Acids Res. 2019;47: D941–D947.
976 doi:10.1093/nar/gky1015

977 54. Park CK, Horton NC. Structures, functions, and mechanisms of filament forming enzymes:
978 a renaissance of enzyme filamentation. Biophys Rev. 2019;11: 927–994.
979 doi:10.1007/s12551-019-00602-6

980 55. Lynch EM, Kollman JM, Webb BA. Filament formation by metabolic enzymes—A new twist
981 on regulation. Curr Opin Cell Biol. 2020;66: 28–33. doi:10.1016/j.ceb.2020.04.006

982 56. Aughey GN, Liu J-L. Metabolic regulation via enzyme filamentation. Crit Rev Biochem Mol
983 Biol. 2016;51: 282–293. doi:10.3109/10409238.2016.1172555

984 57. Simonet JC, Burrell AL, Kollman JM, Peterson JR. Freedom of assembly: metabolic
985 enzymes come together. Bement W, editor. Mol Biol Cell. 2020;31: 1201–1205.
986 doi:10.1091/mbc.E18-10-0675

987 58. Polley S, Lyumkis D, Horton NC. Mechanism of Filamentation-Induced Allosteric Activation
988 of the SgrAI Endonuclease. Structure. 2019;27: 1497-1507.e3.
989 doi:10.1016/j.str.2019.08.001

990 59. Barahona CJ, Basantes LE, Tompkins KJ, Heitman DM, Chukwu BI, Sanchez J, et al. The
991 Need for Speed: Run-On Oligomer Filament Formation Provides Maximum Speed with
992 Maximum Sequestration of Activity. Shisler JL, editor. J Virol. 2019;93: e01647-18.
993 doi:10.1128/JVI.01647-18

994 60. Egelman EH. Actin's prokaryotic homologs. Curr Opin Struct Biol. 2003;13: 244–248.
995 doi:10.1016/S0959-440X(03)00027-7

996 61. Burrell AL, Nie C, Said M, Simonet JC, Fernández-Justel D, Johnson MC, et al. IMPDH1
997 retinal variants control filament architecture to tune allosteric regulation. Nat Struct Mol Biol.
998 2022;29: 47–58. doi:10.1038/s41594-021-00706-2

999 62. Szuba A, Bano F, Castro-Linares G, Iv F, Mavrakis M, Richter RP, et al. Membrane binding
1000 controls ordered self-assembly of animal septins. eLife. 2021;10: e63349.
1001 doi:10.7554/eLife.63349

1002 63. Perkins G, Renken C, Martone ME, Young SJ, Ellisman M, Frey T. Electron Tomography of
1003 Neuronal Mitochondria: Three-Dimensional Structure and Organization of Cristae and
1004 Membrane Contacts. J Struct Biol. 1997;119: 260–272. doi:10.1006/jsbi.1997.3885

1005 64. Liang K, Li N, Wang X, Dai J, Liu P, Wang C, et al. Cryo-EM structure of human mitochondrial
1006 trifunctional protein. Proc Natl Acad Sci. 2018;115: 7039–7044.
1007 doi:10.1073/pnas.1801252115

1008 65. Xia C, Fu Z, Battaile KP, Kim J-JP. Crystal structure of human mitochondrial trifunctional
1009 protein, a fatty acid β-oxidation metabolon. Proc Natl Acad Sci. 2019;116: 6069–6074.
1010 doi:10.1073/pnas.1816317116

1011 66. Zhang M, Zhang L, Guo R, Xiao C, Yin J, Zhang S, et al. Structural basis for the catalytic
1012 activity of filamentous human serine beta-lactamase-like protein LACTB. Structure. 2022;30:
1013 685-696.e5. doi:10.1016/j.str.2022.02.007

1014 67. Booth DS, Avila-Sakar A, Cheng Y. Visualizing Proteins and Macromolecular Complexes by
1015 Negative Stain EM: from Grid Preparation to Image Acquisition. JoVE J Vis Exp. 2011;
1016 e3227. doi:10.3791/3227

1017 68. Mastronarde DN. Automated electron microscope tomography using robust prediction of
1018 specimen movements. J Struct Biol. 2005;152: 36–51. doi:10.1016/j.jsb.2005.07.007

1019 69. Zheng SQ, Palovcak E, Armache J-P, Verba KA, Cheng Y, Agard DA. MotionCor2:
1020 anisotropic correction of beam-induced motion for improved cryo-electron microscopy. Nat
1021 Methods. 2017;14: 331–332. doi:10.1038/nmeth.4193

1022 70. Rohou A, Grigorieff N. CTFFIND4: Fast and accurate defocus estimation from electron
1023 micrographs. J Struct Biol. 2015;192: 216–221. doi:10.1016/j.jsb.2015.08.008

1024 71. Zivanov J, Nakane T, Forsberg BO, Kimanius D, Hagen WJ, Lindahl E, et al. New tools for
1025 automated high-resolution cryo-EM structure determination in RELION-3. Egelman EH,
1026 Kuriyan J, editors. eLife. 2018;7: e42166. doi:10.7554/eLife.42166

1027 72. He S, Scheres SHW. Helical reconstruction in RELION. J Struct Biol. 2017;198: 163–176.
1028 doi:10.1016/j.jsb.2017.02.003

1029 73. Kucukelbir A, Sigworth FJ, Tagare HD. Quantifying the local resolution of cryo-EM density
1030 maps. Nat Methods. 2014;11: 63–65. doi:10.1038/nmeth.2727

1031 74. Jumper J, Evans R, Pritzel A, Green T, Figurnov M, Ronneberger O, et al. Highly accurate
1032 protein structure prediction with AlphaFold. Nature. 2021;596: 583–589.
1033 doi:10.1038/s41586-021-03819-2

1034 75. Pettersen EF, Goddard TD, Huang CC, Couch GS, Greenblatt DM, Meng EC, et al. UCSF
1035 Chimera—A visualization system for exploratory research and analysis. J Comput Chem.
1036 2004;25: 1605–1612. doi:10.1002/jcc.20084

1037 76. Liebschner D, Afonine PV, Baker ML, Bunkóczi G, Chen VB, Croll TI, et al. Macromolecular
1038 structure determination using X-rays, neutrons and electrons: recent developments in
1039 Phenix. Acta Crystallogr Sect Struct Biol. 2019;75: 861–877.
1040 doi:10.1107/S2059798319011471

1041 77. Emsley P, Lohkamp B, Scott WG, Cowtan K. Features and development of Coot. Acta
1042 Crystallogr D Biol Crystallogr. 2010;66: 486–501. doi:10.1107/S0907444910007493

1043 78. Williams CJ, Headd JJ, Moriarty NW, Prisant MG, Videau LL, Deis LN, et al. MolProbity:
1044 More and better reference data for improved all-atom structure validation. Protein Sci.
1045 2018;27: 293–315. doi:10.1002/pro.3330

1046 79. Pettersen EF, Goddard TD, Huang CC, Meng EC, Couch GS, Croll TI, et al. UCSF
1047 ChimeraX: Structure visualization for researchers, educators, and developers. Protein Sci.
1048 2021;30: 70–82. doi:10.1002/pro.3943

1049 80. Schindelin J, Arganda-Carreras I, Frise E, Kaynig V, Longair M, Pietzsch T, et al. Fiji: an
1050 open-source platform for biological-image analysis. Nat Methods. 2012;9: 676–682.
1051 doi:10.1038/nmeth.2019

1052 81. Jurrus E, Engel D, Star K, Monson K, Brandi J, Felberg LE, et al. Improvements to the APBS
1053 biomolecular solvation software suite. Protein Sci. 2018;27: 112–128. doi:10.1002/pro.3280

1054 82. Krissinel E, Henrick K. Inference of Macromolecular Assemblies from Crystalline State. J
1055 Mol Biol. 2007;372: 774–797. doi:10.1016/j.jmb.2007.05.022

1056 83. Holm L, Rosenström P. Dali server: conservation mapping in 3D. Nucleic Acids Res.
1057 2010;38: W545–W549. doi:10.1093/nar/gkq366

1058 84. Nguyen MN, Tan KP, Madhusudhan MS. CLICK—topology-independent comparison of
1059 biomolecular 3D structures. Nucleic Acids Res. 2011;39: W24–W28. doi:10.1093/nar/gkr393

1060 85. Sievers F, Wilm A, Dineen D, Gibson TJ, Karplus K, Li W, et al. Fast, scalable generation
1061 of high-quality protein multiple sequence alignments using Clustal Omega. Mol Syst Biol.
1062 2011;7: 539. doi:10.1038/msb.2011.75

1063 86. Robert X, Gouet P. Deciphering key features in protein structures with the new ENDscript
1064 server. Nucleic Acids Res. 2014;42: W320–W324. doi:10.1093/nar/gku316

1065 87. Ardail D, Privat JP, Egret-Charlier M, Levrat C, Lerme F, Louisot P. Mitochondrial contact
1066 sites. Lipid composition and dynamics. J Biol Chem. 1990;265: 18797–18802.
1067 doi:10.1016/S0021-9258(17)30583-5

1068
1069

1070 ## Supporting Information
1071
1072 **S1 Fig. CryoEM raw data and validation of the human LACTB filament.** (**A**) A representative
1073 cryoEM micrograph and (**B**) 2D class averages of the human LACTB filament. (**C**) Slices through
1074 the unsharpened density map of the LACTB filament are shown in the top view. (**D**) CryoEM map
1075 of the human LACTB filament is colored according to the local resolution estimation calculated by
1076 ResMap. (**E**) Fourier Shell Correlation (FSC) curve shows 3.1 Å global resolution (masked in
1077 purple and unmasked in orange) with the gold standard criteria (FSC=0.143). (**F**) Euler angle
1078 distribution of the segments used in the final 3D reconstruction.
1079
1080 **S2 Fig. LACTB filament data processing strategy.** Flow chart summarizing cryoEM image-
1081 processing workflow, including 3D classification and 3D auto-refinement, CTF refinement, and
1082 Bayesian polishing.
1083
1084 **S3 Fig. CryoEM map quality of the LACTB filament.** (**A**) Fourier Shell Correlation (FSC) curves
1085 for the final helical symmetry imposed (purple line) and C1 symmetry (blue line) 3D
1086 reconstructions. (**B**) 3D Fourier Shell Correlation of the final cryoEM map.
1087
1088 **S4 Fig. Comparison of the LACTB monomer with different structures of homologous**
1089 **proteins and sequence alignment with bacterial PBP-βL family of enzymes.** (**A-D**),
1090 Comparison of human LACTB monomer (green) with *S. aureus* ClbP protein (yellow, PDB ID:
1091 4GDN), *P. abyssi* Pab87 peptidase (orange, PDB ID: 2QMI), *A. halodurans* penicillin-binding
1092 protein (pink, PDB ID: 3TG9), and *B. anthropi* D-amino-acid amidase (purple, PDB ID: 2EFU).
1093 The root-mean-square deviation of each structure relative to the LACTB monomer is shown at
1094 the bottom. While most β-strands align well between human and bacterial proteins, the
1095 surrounding helices and interface-forming loops show significant differences between these

1096 structures. (**E**) Sequence alignment of LACTB homologs and orthologs. Residues that form the
1097 dimerization interface and polymerization interfaces 1 and 2 are highlighted with orange, purple
1098 and blue boxes, respectively. Catalytic site residues are highlighted with an asterisk. Secondary
1099 structure elements shown above the alignment are generated from the human LACTB structure.
1100 Sequences were aligned using Homo Sapiens LACTB (Uniprot ID: P83111), *S. aureus* ClbP
1101 (Uniprot ID: Q7A3Q5), *P. abyssi* Pab87 peptidase (Uniprot ID: Q9V2D6), *A. halodurans* penicillin-
1102 binding protein (Uniprot ID: Q9KAM0), and *B. anthropi* D-amino-acid amidase (Uniprot ID:
1103 Q9LCC8).
1104
1105 **S5 Fig. Structure of LACTB catalytic site and multiple sequence alignment of mammalian**
1106 **LACTB homologs.** (**A**) Active site and ligand recognition of human LACTB. Ribbon diagram of a
1107 monomer is displayed in green and residues forming the catalytic site are shown as sticks. Boxed
1108 zoom images highlight the positions of the conserved residues that contribute to catalytic site
1109 formation. (**B**) Surface electrostatic potential representation of the LACTB monomer. Positive and
1110 negative electrostatic potentials are shown in blue and red, respectively. The substrate binding
1111 cavity is highlighted with a red circle. (**C**) Sequence alignment of LACTB homologs. Residues that
1112 form the dimerization interface and polymerization interfaces 1 and 2 are highlighted with orange,
1113 purple and blue boxes, respectively. Catalytic site residues are highlighted with an asterisk.
1114 Secondary structure elements shown above the alignment are generated from the human LACTB
1115 structure. LACTB sequences from Homo sapiens (human; Uniprot ID: P83111), Pan troglodytes
1116 (chimpanzee; Uniprot ID: K7CYM3), Macaca mulatta (rhesus macaque; Uniprot ID: F7EXQ6),
1117 Mus musculus (mouse; Uniprot ID: Q9EP89), Bos taurus (cow; Uniprot ID: P83095), Equus asinus
1118 (donkey; Uniprot ID: UPI001D03C0DD), Puma concolor (mountain lion; Uniprot ID:
1119 A0A6P6HFT1), and Lontra canadensis (river otter; Uniprot ID: UPI0013F34634) are aligned.
1120

1121 **S6 Fig. SDS-PAGE and negative-stain TEM analyses of LACTB filaments in the presence**
1122 **of H_2O_2.** (**A**) Ribbon diagram of the LACTB monomer is displayed in green, and residues forming
1123 a methionine cluster are shown as sticks. Boxed zoomed in image highlights the positions of
1124 methionine residues which are colored orange and yellow. (**B**) Coomassie blue-stained SDS-
1125 PAGE gel of WT LACTB protein treated with increasing concentrations (0.1%, 0.5%, and 1.0%)
1126 of H_2O_2. Indicated concentrations of H_2O_2 were incubated with purified LACTB for 30 min before
1127 SDS-PAGE analysis. The left lane is the molecular weight standards, and their positions are
1128 indicated. (**C**) Sequence of WT LACTB construct (residues 97-547) with confirmation of
1129 methionine residues oxidized upon exposure to H_2O_2 (shown in red) by liquid chromatography
1130 with tandem mass spectrometry (LC-MS/MS). The underlying data for (**C**) is provided in S2 Data.
1131 (**D**) Representative negative-stain TEM micrographs of WT LACTB treated with varying
1132 concentrations of H_2O_2 for 30 min before grid preparation. Scale bars, 100 nm.
1133
1134 **S7 Fig. Structural characterization of LACTB filaments with liposomes of different**
1135 **compositions and nanotubes.** (**A**) Negative stain images of liposomes with different
1136 compositions. From left to right: PC:PE:PI:CL, PC:PE:PI, PC:PE, PC. (**B**) Negative stain images
1137 of WT LACTB in the presence of liposomes with different compositions in the same order as (**A**).
1138 (**C**) Total liposome binding activity of WT LACTB with liposomes of different compositions. Total
1139 liposome binding was quantified by counting 1000 filaments from at least three independent
1140 reconstitution assays and calculating the total percentage of filament binding. Bars represent the
1141 mean of at least three independent reconstitution assays and error bars indicate the s.e.m. (**D**)
1142 Percentage of LACTB filaments bound to liposomes by interaction type. Bars represent the mean
1143 of at least three independent reconstitution assays and error bars indicate the s.e.m. (**E**) Negative
1144 stain images of empty nanotubes (left) and WT LACTB filaments in the presence of nanotubes
1145 (right). The source data for (**C**) and (**D**) are provided in sheets S7C and S7D Fig in S1 Data.

1146

1147 **S8 Fig. Structural characterization of the lipid binding region of LACTB.** (**A**) Size exclusion
1148 chromatography (SEC) elution profiles of WT and mutant LACTB. SEC elution profiles begin with
1149 the void volume (V_0) of the column. Fractions were analyzed by SDS-PAGE and peak fractions
1150 used in negative-stain analyses are highlighted in red boxes. Negative-stain TEM images
1151 demonstrate the polymerization activity of WT and mutant proteins. Scale bars, 100 nm. (**B**)
1152 Catalytic activity of key residues involved in lipid binding. Enzyme activity was determined *in vitro*
1153 by using a fluorescently labeled substrate and three independent experiments were performed
1154 for each sample. Bars represent the mean of at least three independent experiments and error
1155 bars represent the standard deviation. (**C**) Total liposome binding activity of WT LACTB and key
1156 residues involved in lipid binding. Total liposome binding was quantified by counting 1000
1157 filaments from at least three independent reconstitution assays and calculating the total
1158 percentage of filament binding. Bars represent the mean of at least three independent
1159 reconstitution assays and error bars indicate the s.e.m. The underlying data in (**B**) and (**C**) are
1160 provided in sheets S8B and S8C Fig in S1 data.

1161

1162 **S9 Fig. Computational modeling of LACTB lipid binding motifs to membranes.** The
1163 monomeric structure of WT human LACTB was obtained from AlphaFold and the rotational and
1164 translation position of the protein was calculated in the presence of membranes, mimicking the
1165 lipid composition of the mitochondrial IM using the PPM Web Server. Boxed zoomed in images
1166 highlight the predicted structures of ^{259}KNxFxKFK^{266} and ^{274}KxRxxKxxKKK^{284} motifs within the
1167 flexible loop region (L6) of human LACTB.

1168

1169 **S10 Fig. Mechanistic model describing LACTB assembly mechanism within mitochondria.**
1170 After being imported to mitochondrial IMS, LACTB protomers assemble into antiparallel dimers.

1171 Subsequently, LACTB dimers interact through two polymerization interfaces, which allow the
1172 stacking of antiparallel dimers in a helical fashion and lead to the polymerization into micron-scale
1173 helical assemblies. Upon filament formation, LACTB gains catalytic activity and filament
1174 elongation increases the catalytic efficiency of the enzyme.
1175
1176 **S1 Table. Disease-associated missense mutations in human LACTB.** Mutations associated
1177 with various cancers were compiled from the Catalogue of Somatic Mutations in Cancer
1178 (COSMIC), the Genome Aggregation Database (gnomAD), and The Cancer Genome Atlas
1179 Program (TCGA).
1180
1181 **S1 Data. The numerical values underlying Figs 1F and 3D and 4E and 5G-I and S7C-D and**
1182 **S8B-C**. (XLSX). Sheets show the values underlying the data displayed in all figures and includes
1183 an explanation of all data. Sheet Fig 1F shows the raw data from *in vitro* substrate fluorescence
1184 assays for WT LACTB underlying Fig 1F. Sheet Fig 3D details the raw data from *in vitro* substrate
1185 fluorescence assays for LACTB mutants underlying Fig 3D. Sheet Fig 4E describes the raw data
1186 from *in vitro* substrate fluorescence assays for LACTB mutants underlying Fig 4E. Sheet Fig 5G
1187 shows the raw data from *in vitro* substrate fluorescence assays in the presence of liposomes
1188 underlying Fig 5G. Sheet Fig 5H describes the raw data from LACTB membrane binding assays
1189 based on membrane composition underlying Fig 5H. Sheet Fig 5I reports the raw data from
1190 LACTB membrane binding assays for LACTB mutants underlying Fig 5I. Sheet S7C Fig
1191 represents the raw data from LACTB membrane binding assays based on membrane composition
1192 underlying S7C Fig. Sheet S7D Fig shows the raw data from LACTB membrane binding assays
1193 for WT LACTB based on binding classification underlying S7D Fig. Sheet S8B Fig details the raw
1194 data from *in vitro* substrate fluorescence assays for LACTB mutants underlying S8B Fig. Sheet

1195 S8C Fig describes the raw data from LACTB membrane binding assays for LACTB mutants
1196 underlying S8C Fig.
1197
1198 **S2 Data. Source data of liquid chromatography with tandem mass spectrometry (LC-**
1199 **MS/MS) in S6C Fig.** (XLSX). Parameters sheet shows the experimental parameters for LC-
1200 MS/MS experiments of WT LACTB in the presence of H_2O_2. Summary sheet describes the
1201 summary of experimental data for LC-MS/MS experiments. Evidence sheet shows protein
1202 sequence information for LC-MS/MS experiments. Protein Groups sheet details protein identity
1203 information for LC-MS/MS experiments.
1204
1205 **S1 Raw Images. Uncropped images of SDS-PAGE gels of Figs 1C and 3C and 4D and S6B**
1206 **and S8A.** (PDF). Contains raw images for Fig 1C, Fig 3C, Fig 4D, S6B Fig, and S8A Fig.
1207

Fig 1

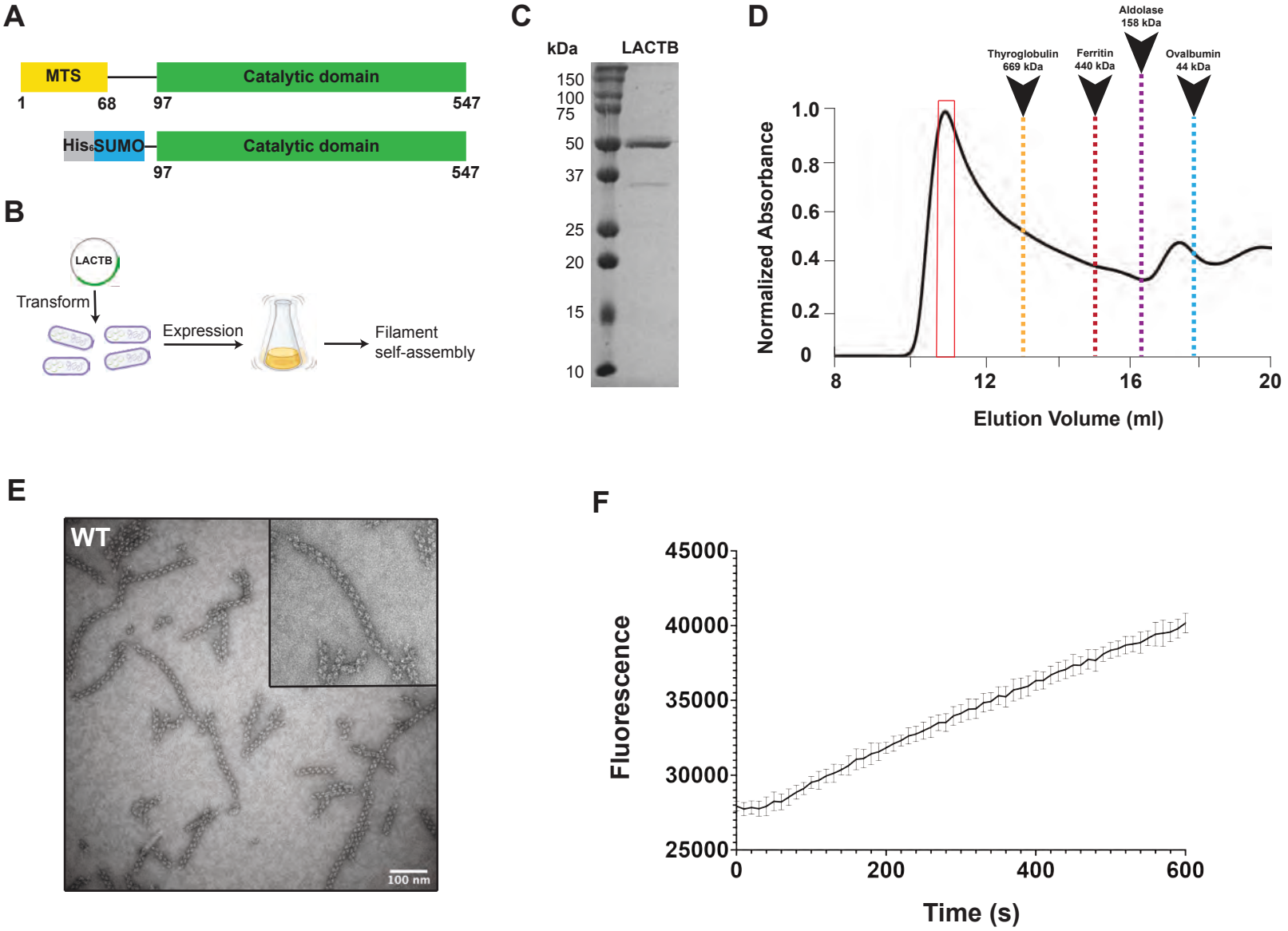
A
MTS
Catalytic domain
1
68
97
547
His6SUMO
Catalytic domain
97
547
B
LACTB
Transform
Expression
Filament
self-assembly
C
kDa
LACTB
150
100
75
50
37
25
20
15
10
D
Aldolase
158 kDa
Thyroglobulin
669 kDa
Ferritin
440 kDa
Ovalbumin
44 kDa
Normalized Absorbance
1.0
0.8
0.6
0.4
0.2
0
8
12
16
20
Elution Volume (ml)
E
WT
100 nm
F
Fluorescence
45000
40000
35000
30000
25000
0
200
400
600
Time (s)

Fig 2

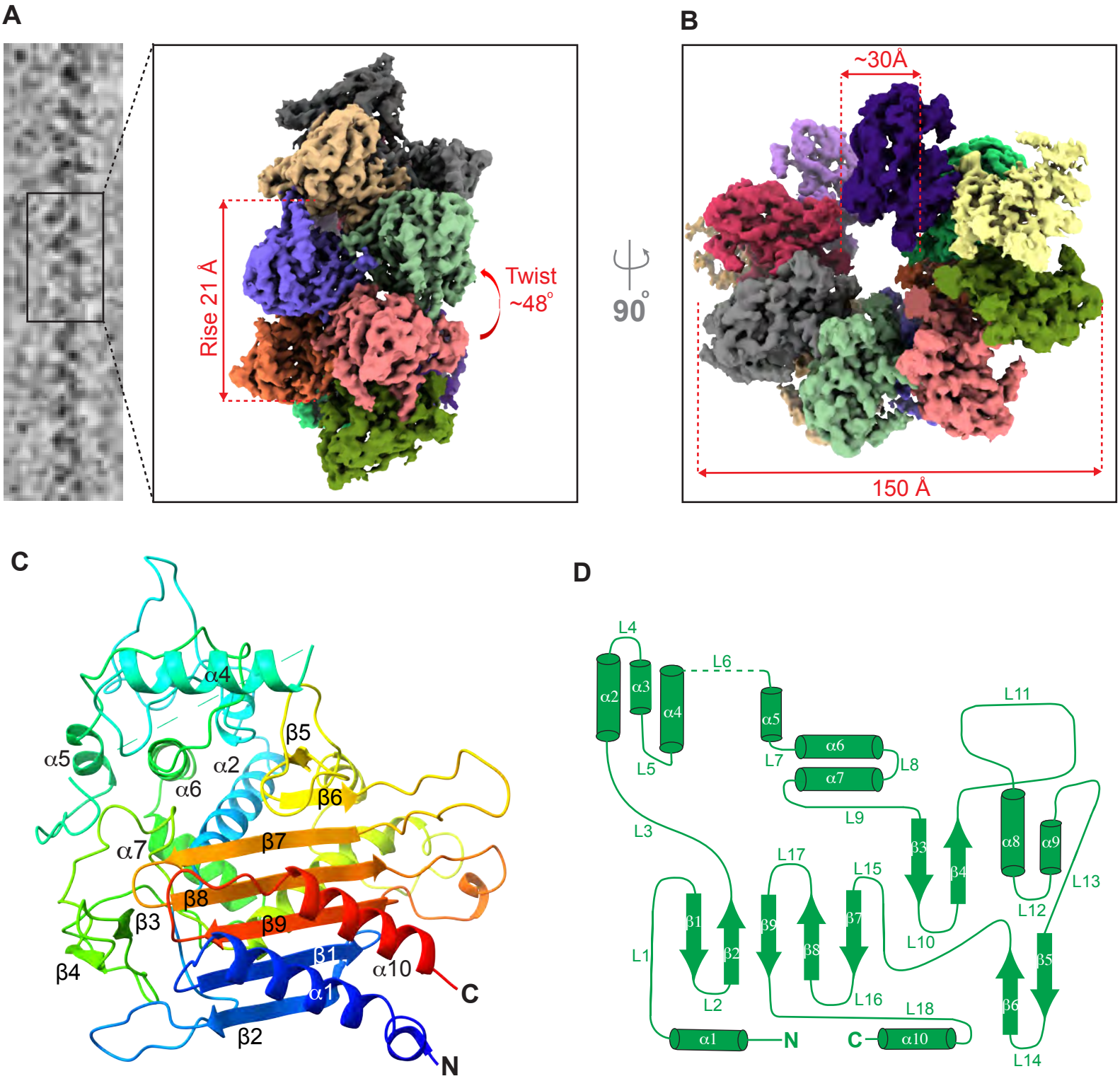
A
Rise 21 Å
Twist
~48°
90°
B
~30Å
150 Å
C
α4
α5
α2
β5
α6
β6
α7
β7
β8
β3
β9
β4
β1
α10
α1
β2
C
N
D
L4
L6
α2
α3
α4
α5
L5
L7
α6
α7
L8
L9
L11
L3
β3
β4
α8
α9
L13
L17
L15
L12
β1
β9
β7
L1
β2
β8
L10
β5
L2
L16
L18
β6
α1
N
C
α10
L14

Fig 3

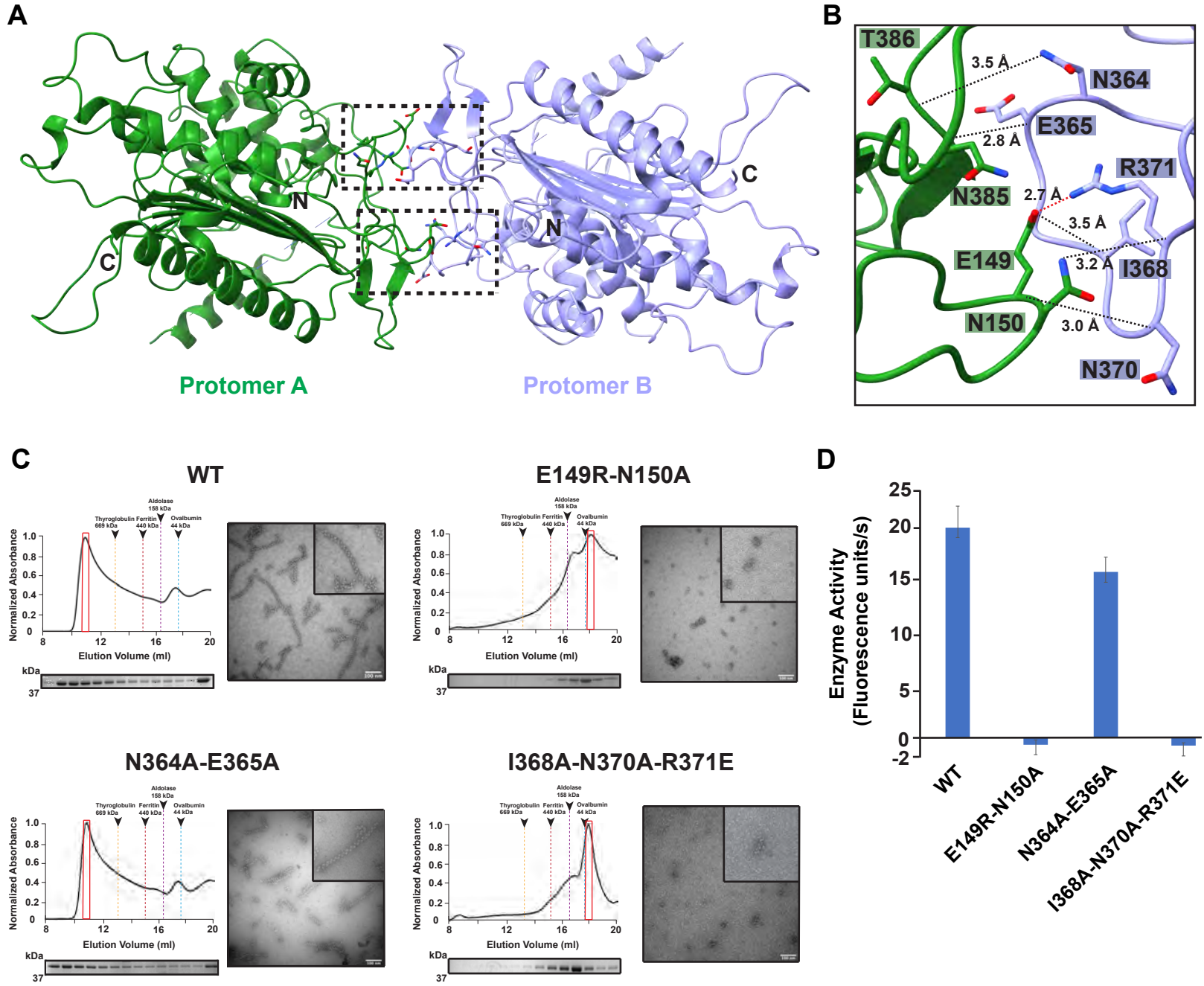
A
N
C
N
C
Protomer A
Protomer B
B
T386
3.5 Å
N364
E365
2.8 Å
R371
N385
2.7 Å
3.5 Å
E149
3.2 Å
I368
N150
3.0 Å
N370
C
WT
E149R-N150A
N364A-E365A
I368A-N370A-R371E
Aldolase 158 kDa
Thyroglobulin 669 kDa
Ferritin 440 kDa
Ovalbumin 44 kDa
Normalized Absorbance
Elution Volume (ml)
kDa
37
D
Enzyme Activity (Fluorescence units/s)
WT
E149R-N150A
N364A-E365A
I368A-N370A-R371E

Fig. 4

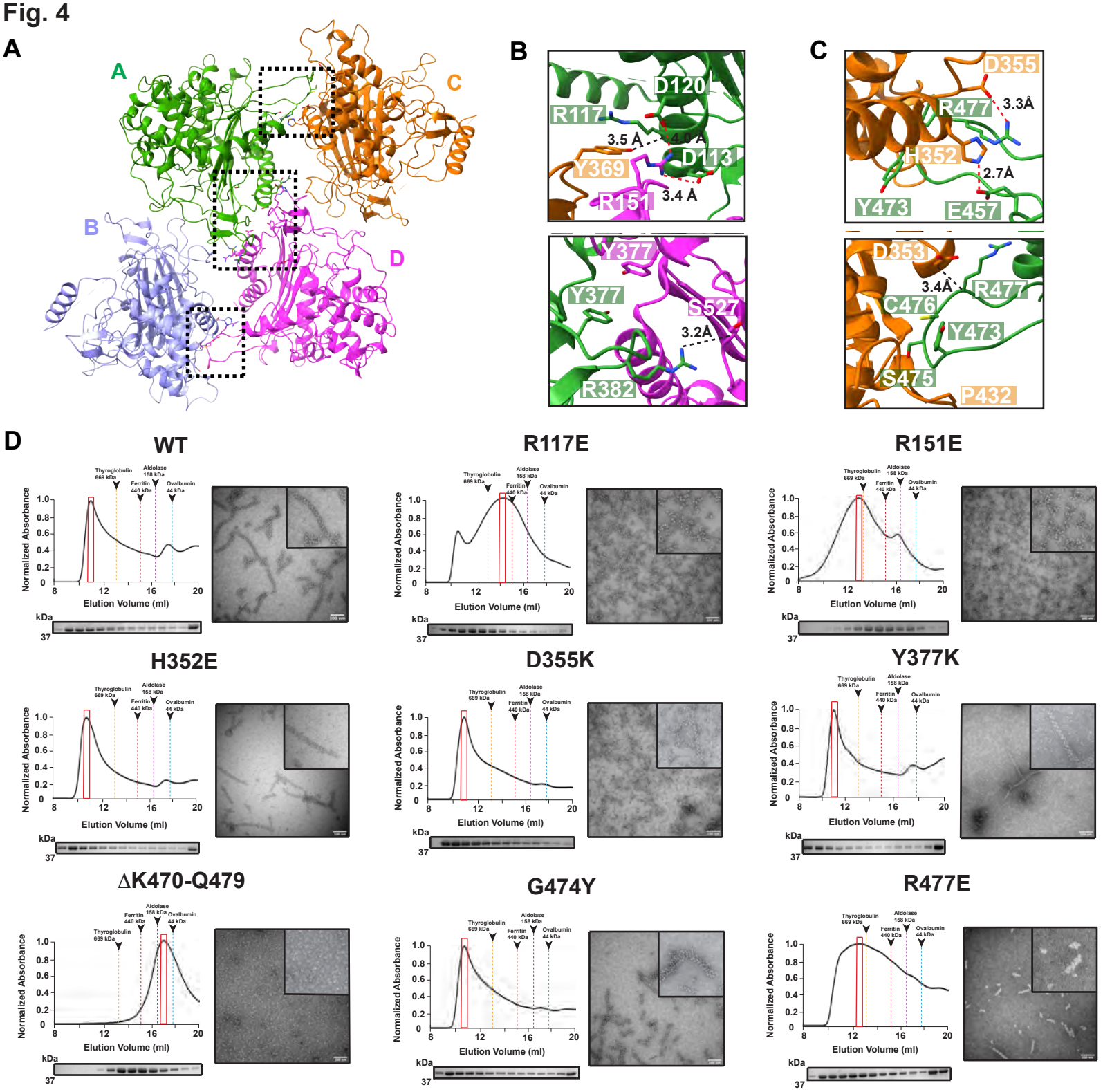
A
A
B
C
D
B
D120
R117
3.5 Å
4.0 Å
D113
Y369
R151
3.4 Å
Y377
Y377
S527
3.2Å
R382
C
D355
R477
3.3Å
H352
2.7Å
Y473
E457
D353
3.4Å
R477
C476
Y473
S475
P432
D
WT
R117E
R151E
H352E
D355K
Y377K
ΔK470-Q479
G474Y
R477E
Thyroglobulin 669 kDa
Aldolase 158 kDa
Ferritin 440 kDa
Ovalbumin 44 kDa
Normalized Absorbance
Elution Volume (ml)
kDa
37
E
Enzyme Activity (Fluorescence units/s)
25
20
15
10
5
0
-2
-5
WT
R117E
R151E
H352E
D355K
Y377K
ΔK470-Q479
G474Y
R477E

Fig 5

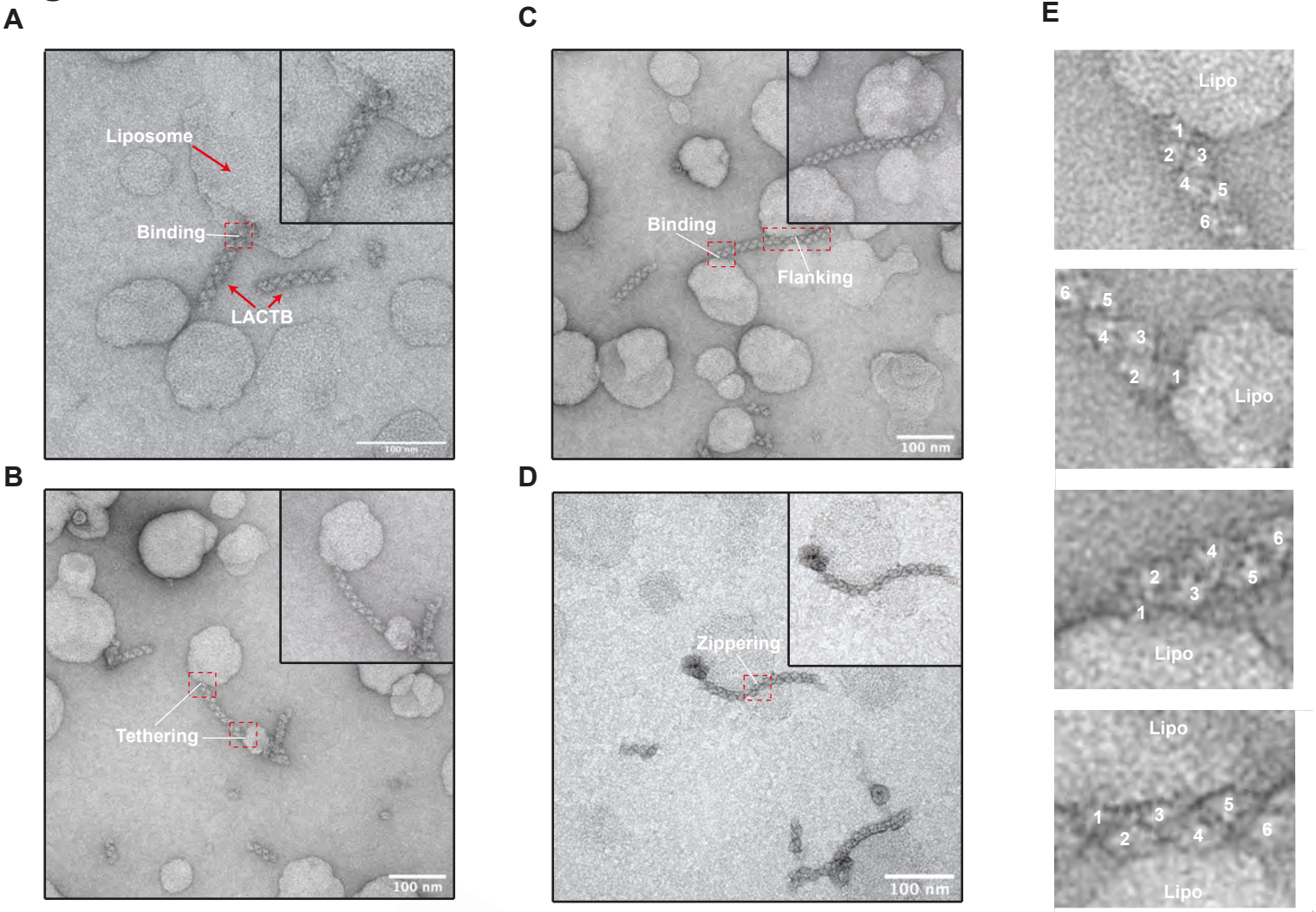
A
Liposome
Binding
LACTB
100 nm
B
Tethering
100 nm
C
Binding
Flanking
100 nm
D
Zippering
100 nm
E
Lipo
1
2
3
4
5
6
Lipo
Lipo
Lipo

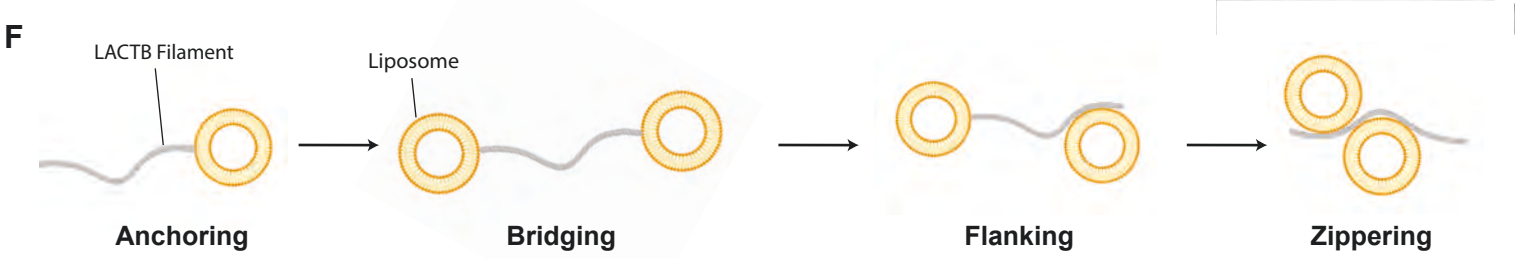
F
LACTB Filament
Liposome
Anchoring
Bridging
Flanking
Zippering

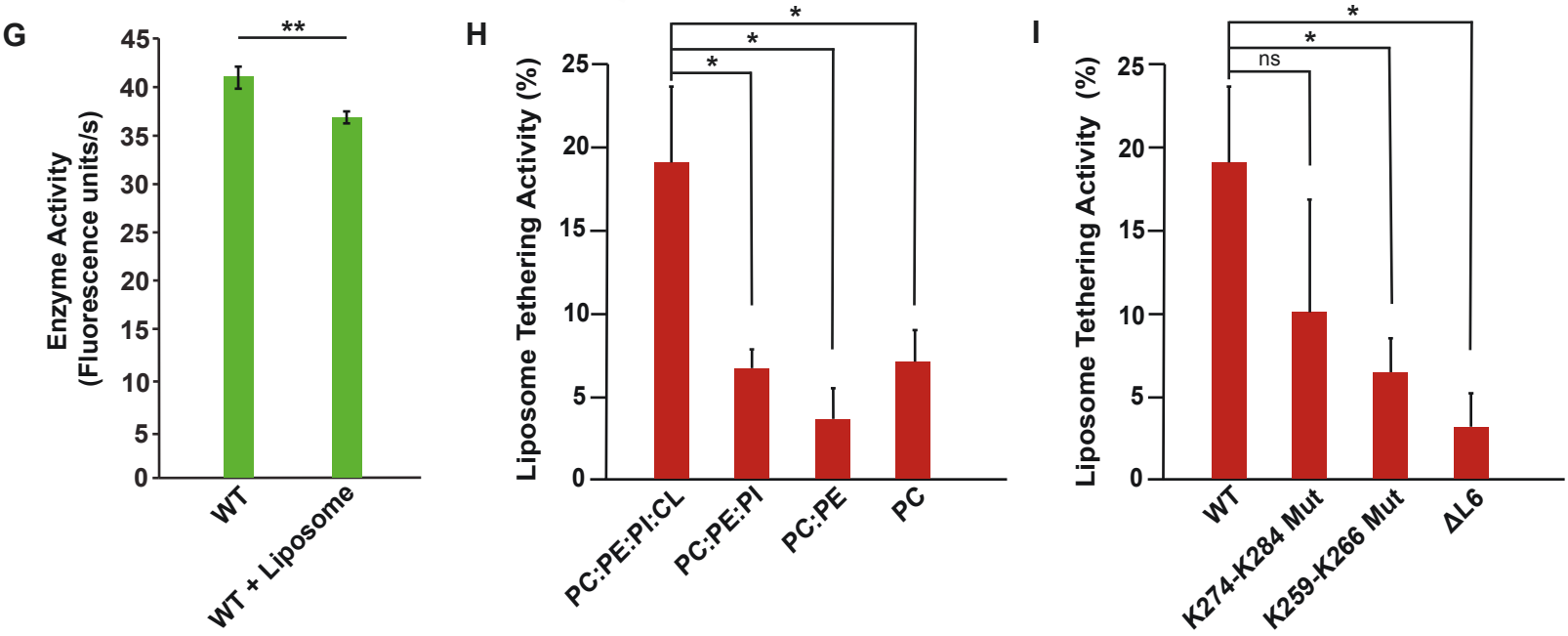
G
Enzyme Activity
(Fluorescence units/s)
45
40
35
30
25
20
15
10
5
0
**
WT
WT + Liposome
H
Liposome Tethering Activity (%)
25
20
15
10
5
0
*
*
*
PC:PE:PI:CL
PC:PE:PI
PC:PE
PC
I
Liposome Tethering Activity (%)
25
20
15
10
5
0
*
*
ns
WT
K274-K284 Mut
K259-K266 Mut
ΔL6

Fig 6

A

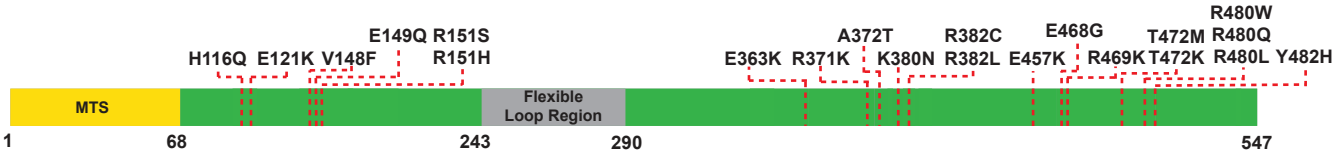
H116Q
E121K
V148F
E149Q
R151S
R151H
E363K
R371K
A372T
K380N
R382C
R382L
E457K
E468G
R469K
T472M
T472K
R480W
R480Q
R480L
Y482H
MTS
Flexible Loop Region
1
68
243
290
547

B

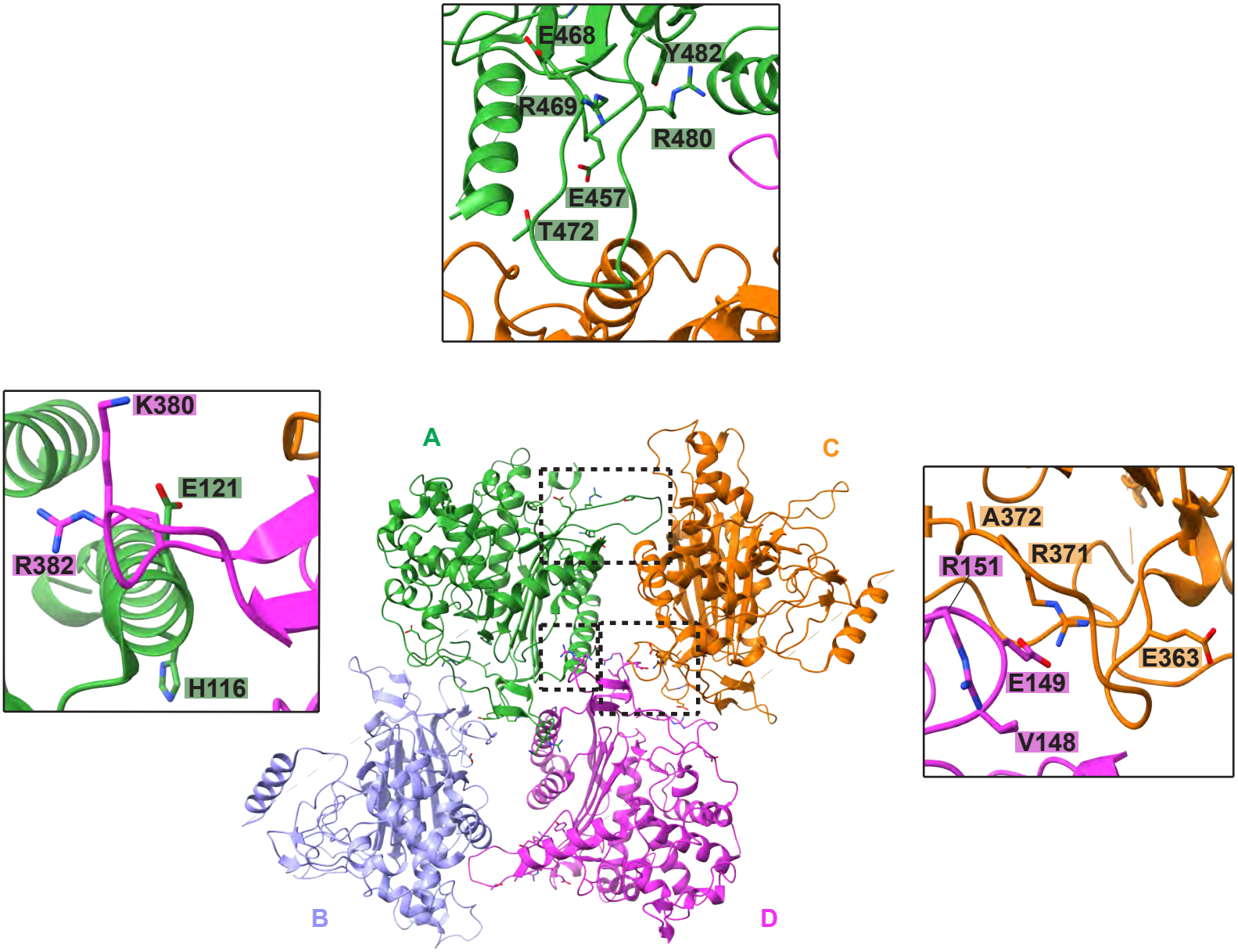
E468
Y482
R469
R480
E457
T472
K380
E121
R382
H116
A
C
B
D
A372
R371
R151
E363
E149
V148

S1 Fig

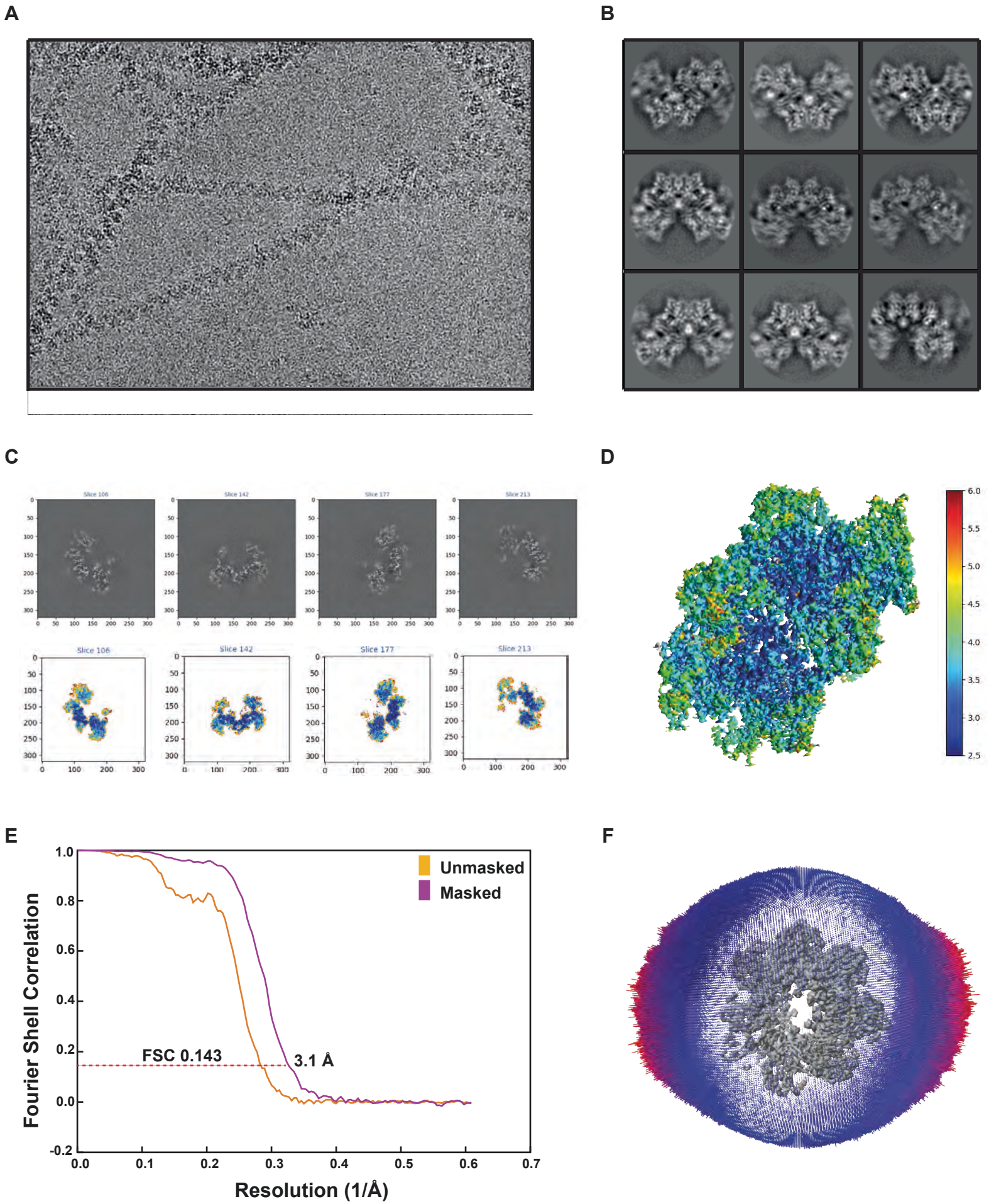
A
B
C
Slice 106
Slice 142
Slice 177
Slice 213
D
6.0
5.5
5.0
4.5
4.0
3.5
3.0
2.5
E
Unmasked
Masked
FSC 0.143
3.1 Å
Fourier Shell Correlation
Resolution (1/Å)
F

S2 Fig

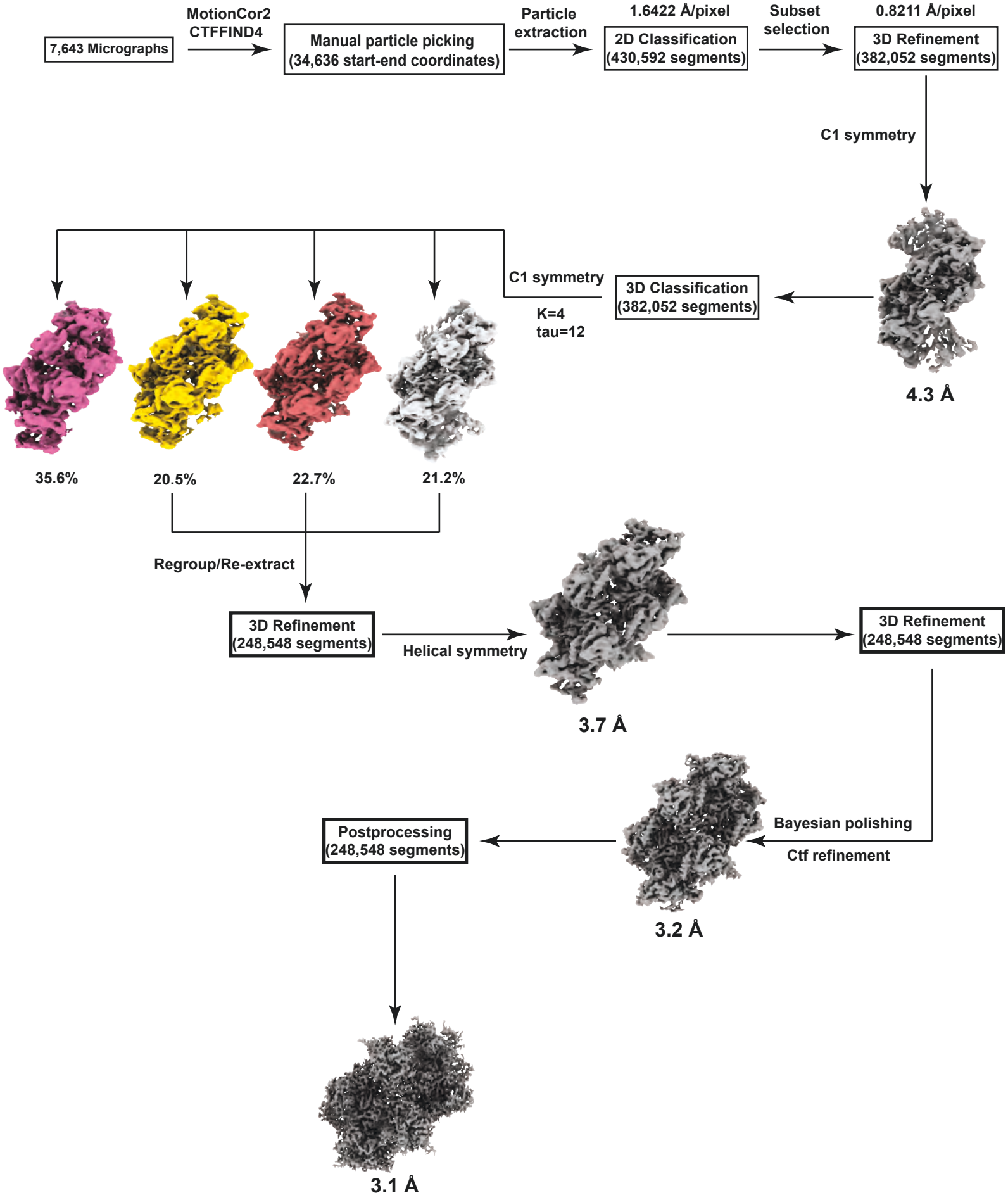
7,643 Micrographs
MotionCor2
CTFFIND4
Manual particle picking
(34,636 start-end coordinates)
Particle
extraction
1.6422 Å/pixel
2D Classification
(430,592 segments)
Subset
selection
0.8211 Å/pixel
3D Refinement
(382,052 segments)
C1 symmetry
4.3 Å
3D Classification
(382,052 segments)
C1 symmetry
K=4
tau=12
35.6%
20.5%
22.7%
21.2%
Regroup/Re-extract
3D Refinement
(248,548 segments)
Helical symmetry
3.7 Å
3D Refinement
(248,548 segments)
Bayesian polishing
Ctf refinement
3.2 Å
Postprocessing
(248,548 segments)
3.1 Å

S3 Fig

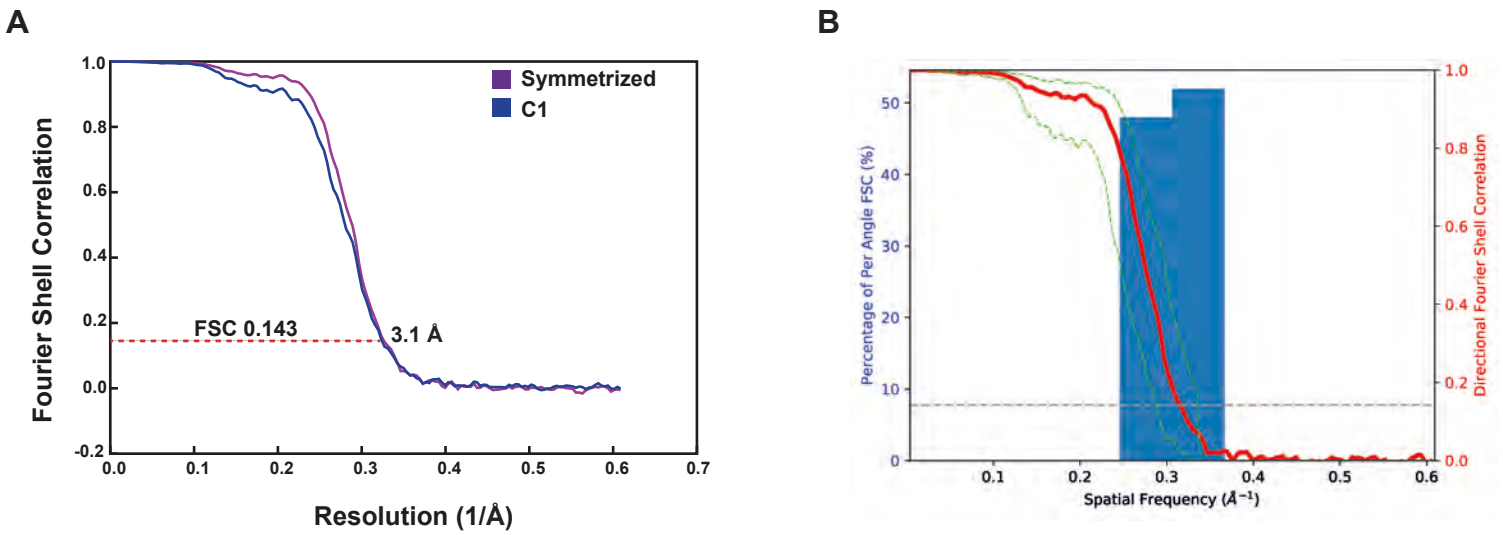
A
Symmetrized
C1
FSC 0.143
3.1 Å
Fourier Shell Correlation
Resolution (1/Å)
B
Percentage of Per Angle FSC (%)
Directional Fourier Shell Correlation
Spatial Frequency (Å⁻¹)

S4 Fig

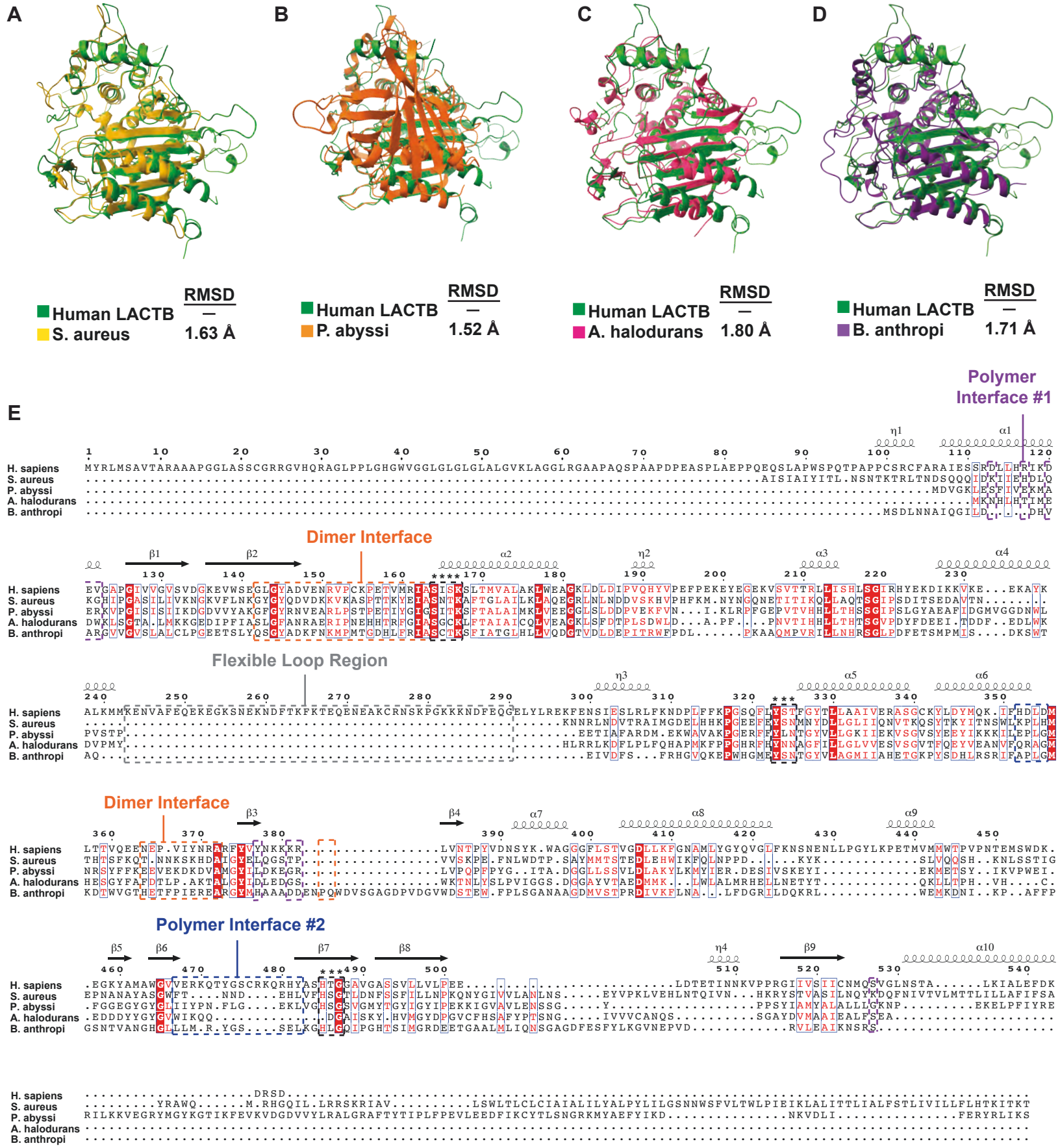
A
B
C
D
Human LACTB
S. aureus
RMSD
1.63 Å
Human LACTB
P. abyssi
RMSD
1.52 Å
Human LACTB
A. halodurans
RMSD
1.80 Å
Human LACTB
B. anthropi
RMSD
1.71 Å
E
Polymer Interface #1
Dimer Interface
Flexible Loop Region
Dimer Interface
Polymer Interface #2
H. sapiens
S. aureus
P. abyssi
A. halodurans
B. anthropi

S5 Fig

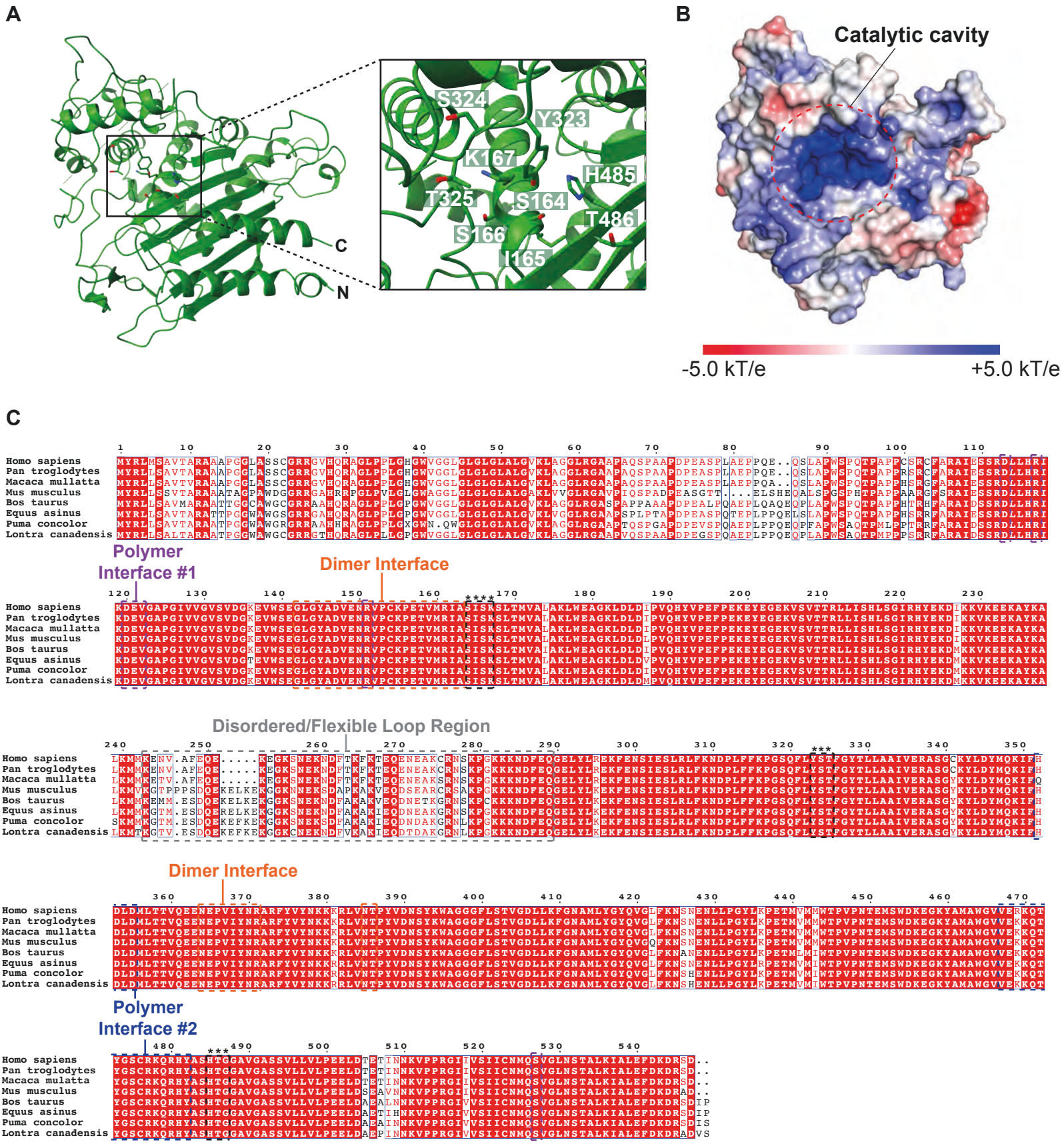
A
C
N
S324
Y323
K167
H485
T325
S164
T486
S166
I165
B
Catalytic cavity
-5.0 kT/e
+5.0 kT/e
C
Homo sapiens
Pan troglodytes
Macaca mullatta
Mus musculus
Bos taurus
Equus asinus
Puma concolor
Lontra canadensis
Polymer Interface #1
Dimer Interface
Disordered/Flexible Loop Region
Dimer Interface
Polymer Interface #2

S6 Fig

A

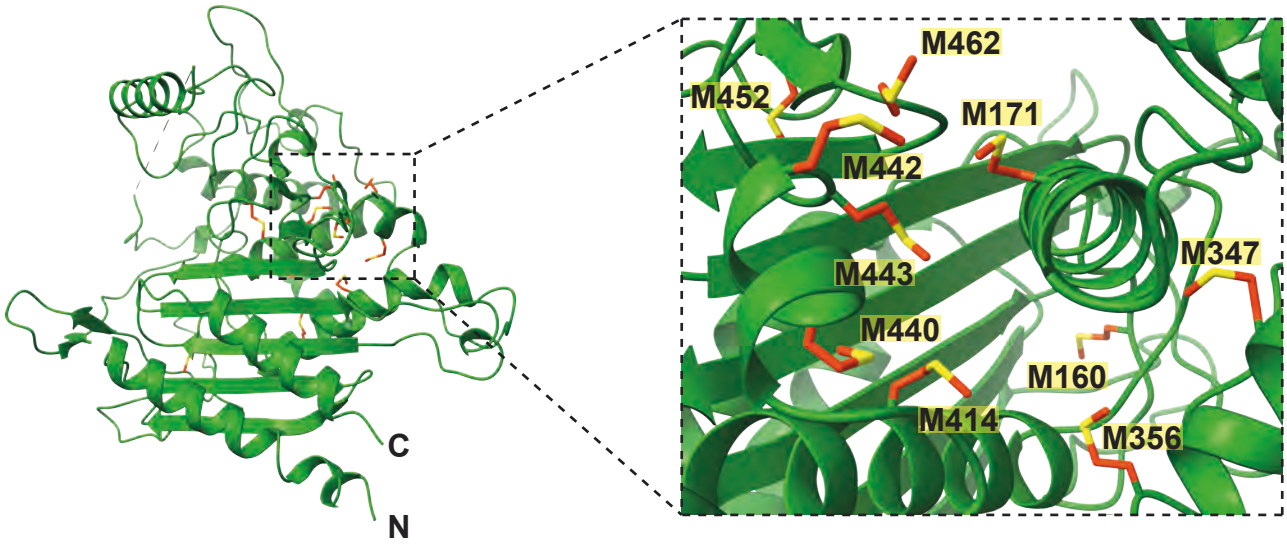

B

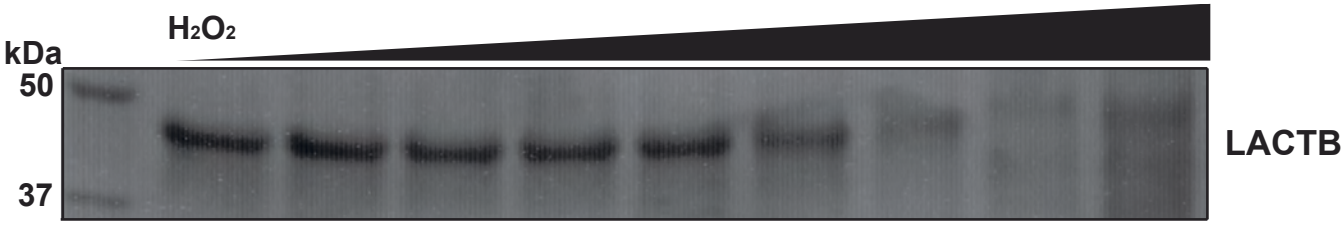

C

```
97   APPCSRCFARAIESSRDLLHRIKDEVGAPGIVVGVSVDGKEVWSEGLGYADVENRVPCKPETVMRIASISKSLTMVALA   175
176  KLWEAGKLDLDIPVQHYVPEFPEKEYEGEKVSVTTRLLISHLSGIRHYEKDIKKVKEEKAYKALKMMKENVAFEQEKEGK   255
256  SNEKNDFTKFKTEQENEAKCRNSKPGKKKNDFEQGELYLREKFENSIESLRLFKNDPLFFKPGSQFLYSTFGYTLLAAIV   335
336  ERASGCKYLDYMQKIFHDLDMLTTVQEENEPVIYNRARFYVYNKKKRLVNTPYVDNSYKWAGGGFLSTVGDLLKFGNA   413
414  MLYGYQVGLFKNSNENLLPGYLKPETMVMMWTPVPNTEMSWDKEGKYAMAWGVVERKQTYGSCRKQRHYASHTGG   488
489  AVGASSVLLVLPEELDTETINNKVPPRGIIVSIICNMQSVGLNSTALKIALEFDKDRSD   547
```

D

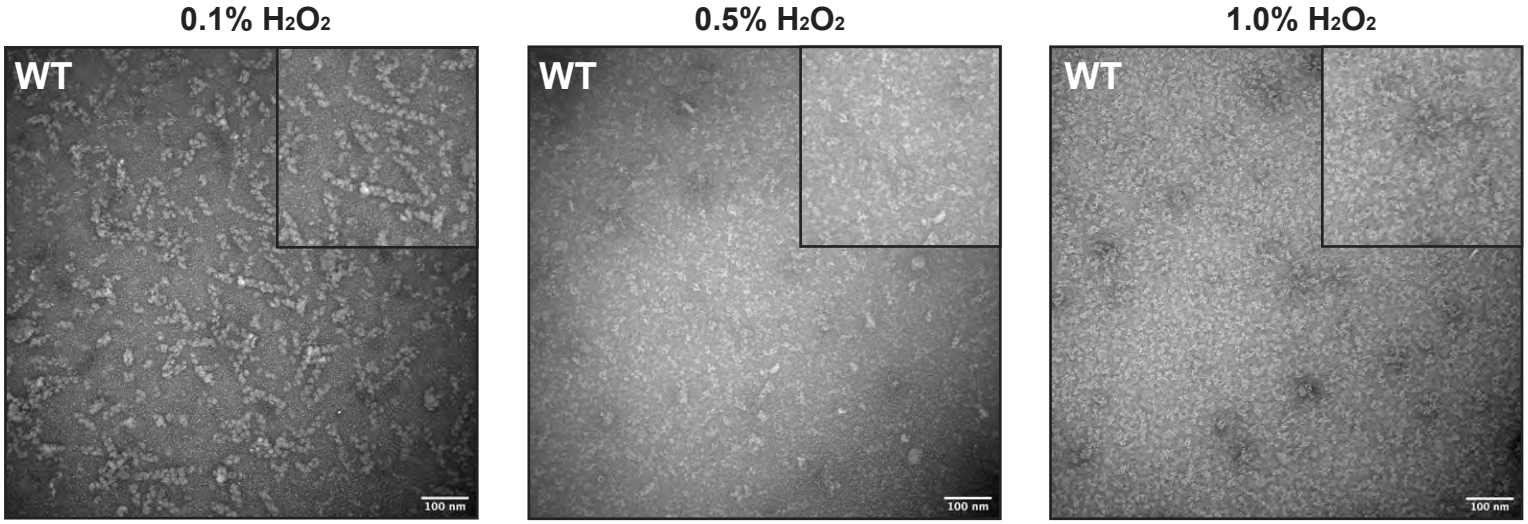

S7 Fig

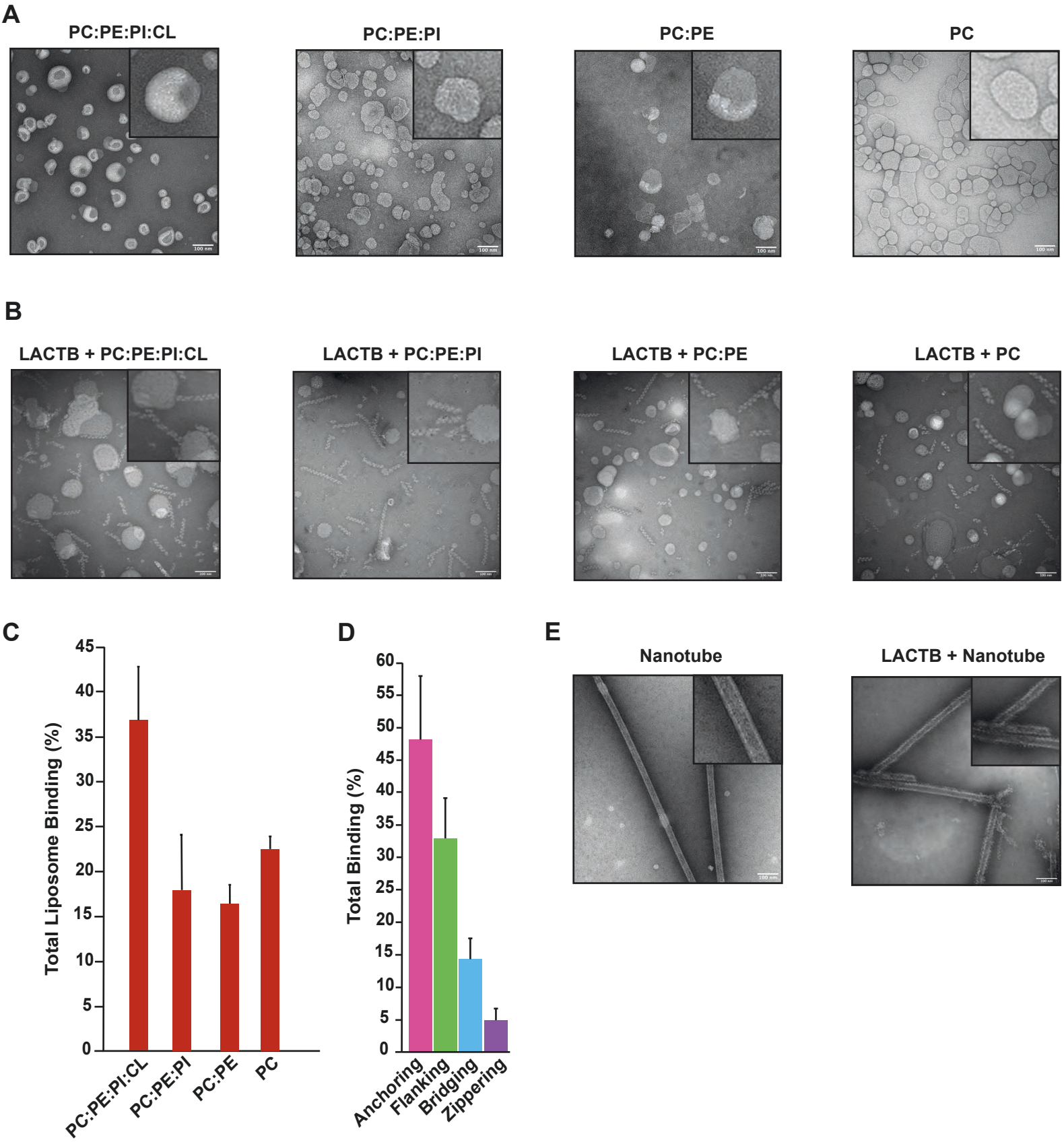
A
PC:PE:PI:CL
PC:PE:PI
PC:PE
PC
B
LACTB + PC:PE:PI:CL
LACTB + PC:PE:PI
LACTB + PC:PE
LACTB + PC
C
Total Liposome Binding (%)
0
5
10
15
20
25
30
35
40
45
PC:PE:PI:CL
PC:PE:PI
PC:PE
PC
D
Total Binding (%)
0
5
10
15
20
25
30
35
40
45
50
55
60
Anchoring
Flanking
Bridging
Zippering
E
Nanotube
LACTB + Nanotube

S8 Fig

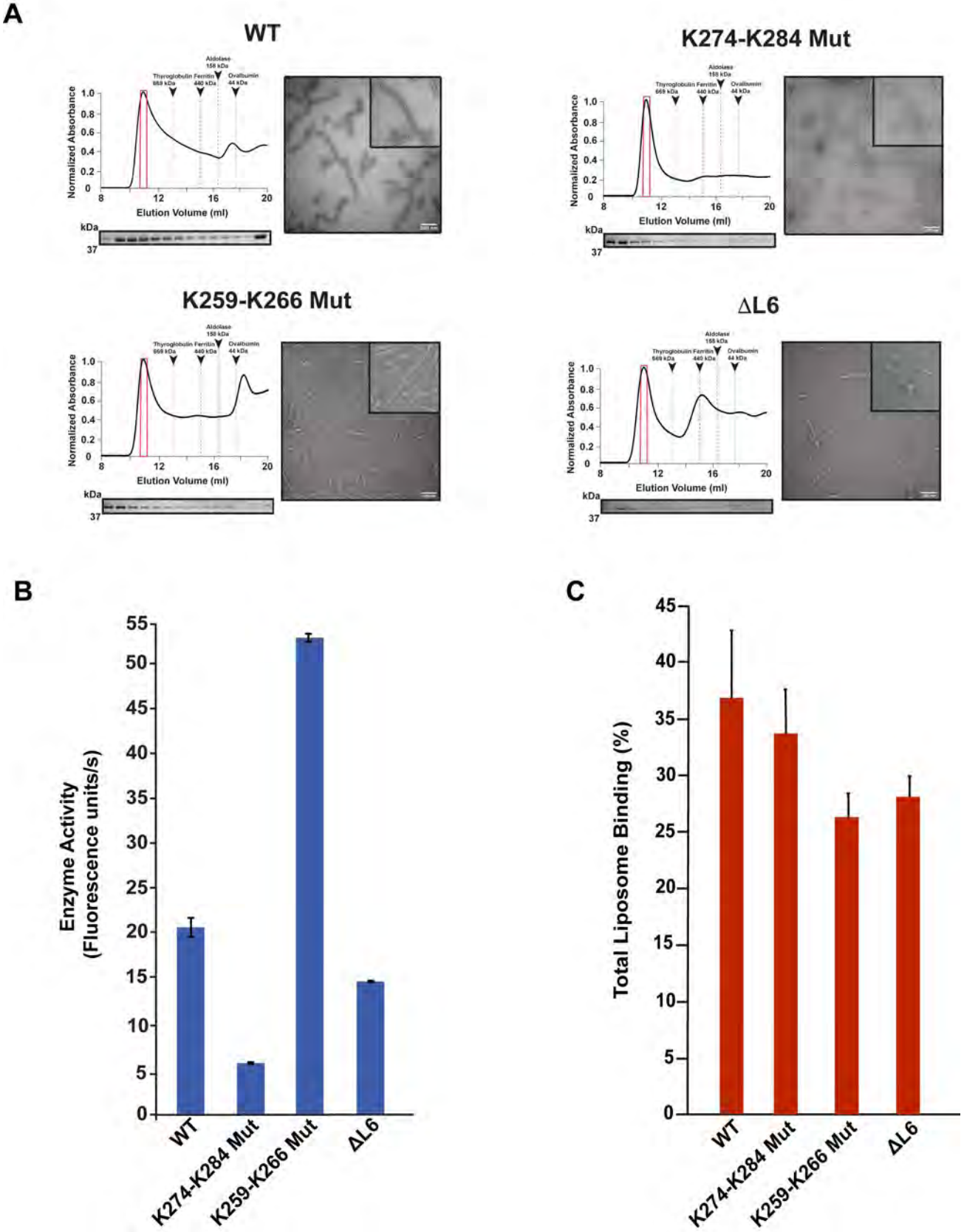
A
WT
K274-K284 Mut
K259-K266 Mut
ΔL6
Aldolase 158 kDa
Thyroglobulin 669 kDa
Ferritin 440 kDa
Ovalbumin 44 kDa
Normalized Absorbance
Elution Volume (ml)
kDa
37
B
Enzyme Activity (Fluorescence units/s)
WT
K274-K284 Mut
K259-K266 Mut
ΔL6
C
Total Liposome Binding (%)
WT
K274-K284 Mut
K259-K266 Mut
ΔL6

S9 Fig

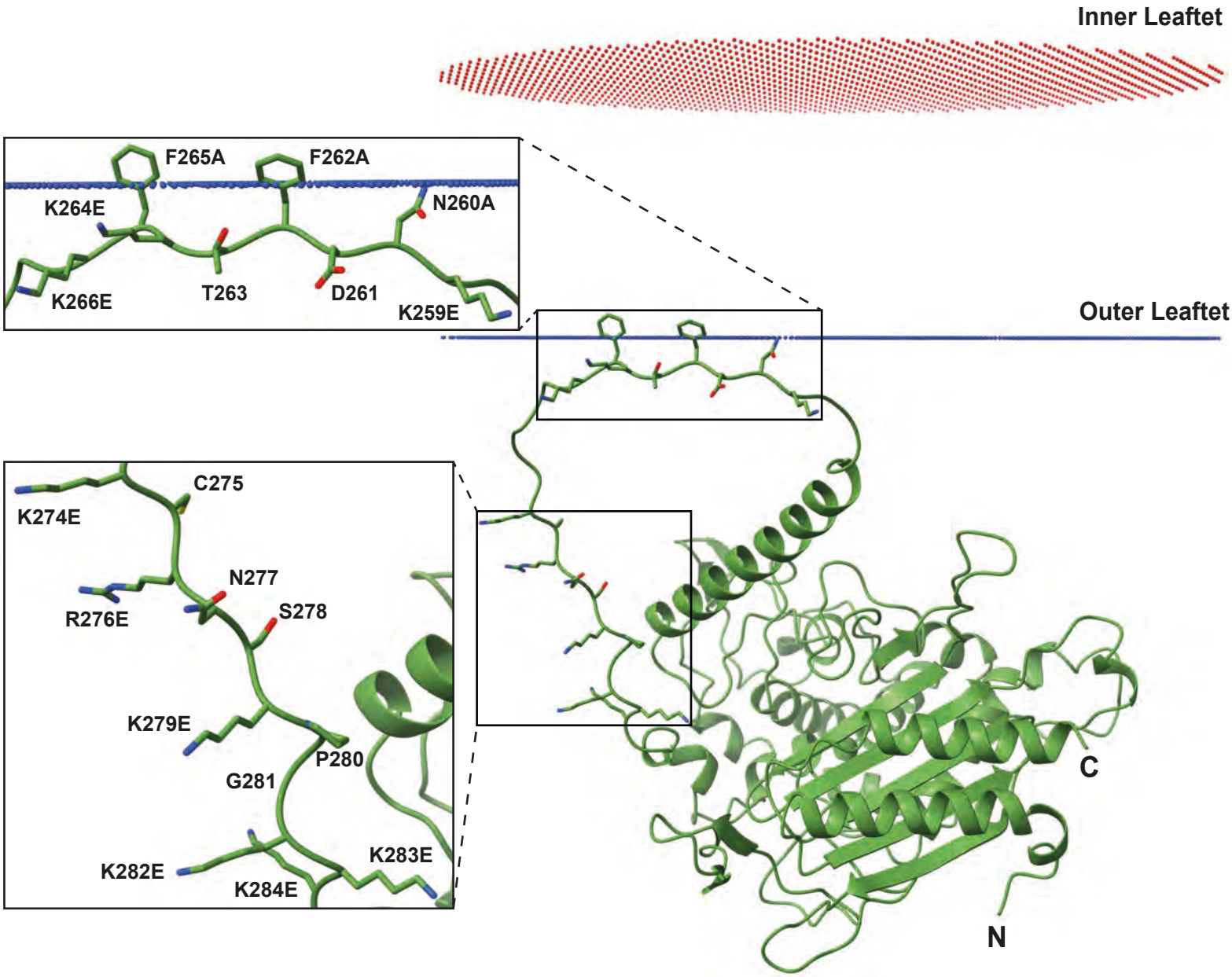
Inner Leaftet
F265A
F262A
K264E
N260A
K266E
T263
D261
K259E
Outer Leaftet
C275
K274E
N277
R276E
S278
K279E
P280
G281
K283E
K282E
K284E
C
N

S10 Fig

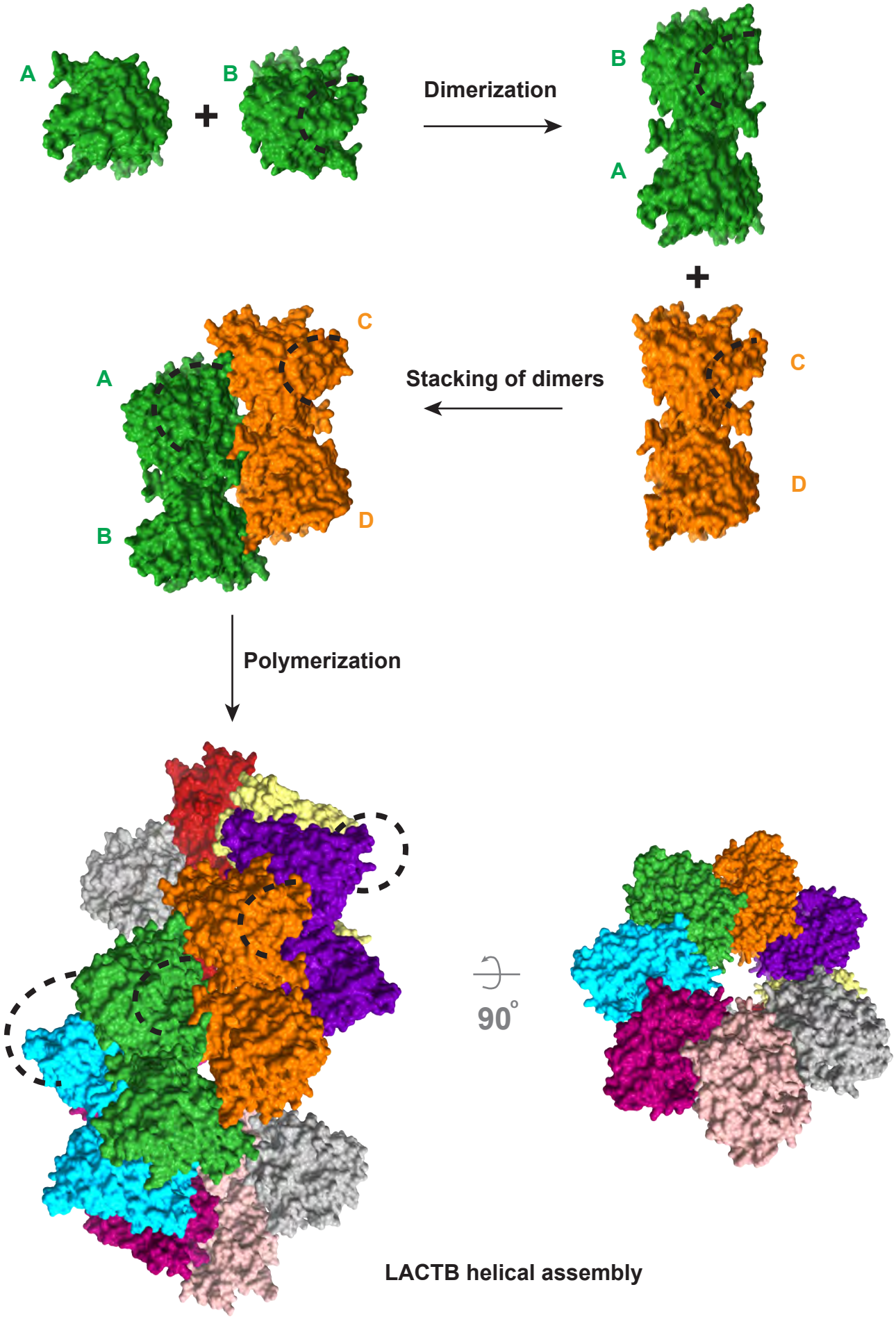
A
B
Dimerization
B
A
C
A
Stacking of dimers
C
D
B
D
Polymerization
90°
LACTB helical assembly

S1 Table | Human LACTB mutations associated with cancer

Protein change	Clinical classification	Cancer type
H116Q	Neutral	Thyroid carcinoma
E121K	Pathogenic	Breast
V148F	Pathogenic	Kidney
E149Q	Pathogenic	Esophagus
R151S, R151H	Likely pathogenic	Uterus
E363K	Pathogenic	Pancreatic
R371K	Pathogenic	Lung
A372T	Pathogenic	Uterus
K380N	Pathogenic	Cervical
R382L, R382C	Pathogenic	Oral, uterus
E457K	Pathogenic	Bladder
E468G	Pathogenic	Glioma
R469K	Pathogenic	Colon, breast
T472K, T472M	Neutral	Melanoma, colon
R480W, R480Q, R480L	Pathogenic	Lung, colon, liver
Y482H	Pathogenic	Melanoma

Mutations associated with cancer were compiled from the Catalogue of Somatic Mutations In Cancer (COSMIC), the Genome Aggregation Database (gnomAD), and The Cancer Genome Atlas Program (TCGA).